

**FATIGUE CRACK GROWTH BEHAVIOUR OF AA6013 ALUMINUM
ALLOY AT DIFFERENT AGING CONDITIONS**

**A THESIS SUBMITTED TO
THE GRADUATE SCHOOL OF NATURAL AND APPLIED SCIENCES
OF
MIDDLE EAST TECHNICAL UNIVERSITY**

BY

AZİZ EGEMEN VARLI

**IN PARTIAL FULFILLMENT OF THE REQUIREMENTS
FOR
THE DEGREE OF MASTER OF SCIENCE
IN
METALLURGICAL AND MATERIALS ENGINEERING**

AUGUST 2006

Approval of the Graduate School of Natural and Applied Sciences.

Prof. Dr. Canan ÖZGEN

Director

I certify that this thesis satisfies all the requirements as a thesis for the degree of Master of Science.

Prof. Dr. Tayfur ÖZTÜRK

Head of Department

This is to certify that we have read this thesis and that in our opinion it is fully adequate, in scope and quality, as a thesis for the degree of Master of Science.

Prof. Dr. Rıza GÜRBÜZ

Supervisor

Examining Committee Members

Prof. Dr. Bilgehan ÖGEL (METU,METE) _____

Prof. Dr. Rıza GÜRBÜZ (METU,METE) _____

Assoc. Prof. Dr. C. Hakan GÜR (METU,METE) _____

Assist. Prof. Dr.Arcan DERİCİOĞLU (METU,METE) _____

Dr. Süleyman YALÇIN (KOMPOZİTEK Ltd. Şti.) _____

I hereby declare that all information in this document has been obtained and presented in accordance with academic rules and ethical conduct. I also declare that, as required by these rules and conduct, I have fully cited and referenced all material and results that are not original to this work.

Name, Last name: Aziz Egemen Varlı

Signature :

ABSTRACT

FATIGUE CRACK GROWTH BEHAVIOUR OF AA6013 ALUMINUM ALLOY AT DIFFERENT AGING CONDITIONS

VARLI, Aziz Egemen

M.S., Department of Metallurgical and Materials Engineering

Supervisor: Prof. Dr. Rıza GÜRBÜZ

August 2006, 84 pages

The effect of different aging treatments on fatigue crack growth behavior of AA6013 aluminum alloy was investigated. C(T) (Compact Tension) specimens were prepared in L-T and T-L direction for fatigue crack growth tests. Samples were in T651 as received, T42 which is solution heat treated at 538 °C for 90 minutes, water quenched and aged in room temperature for 96 hours, and one group of samples were overaged at 245 °C for 12 hours after T42 condition was achieved. Hardness and conductivity measurements were achieved for all conditions after the heat treatments.

Fatigue crack growth tests were performed at as received condition T651, T42 and 245 °C aged samples in laboratory air with sinusoidal loading of stress ratio $R=0.1$ and at a frequency of 1 Hz. The highest fatigue crack growth resistance is observed for T651 T-L and 245 °C overaged L-T condition.

Keywords: Fatigue crack growth rate, compact tension, crack length, stress intensity range, AA6013, aging.

ÖZ

FARKLI YAŞLANDIRMA KOŞULLARINDA AA6013 ALUMİNYUM ALAŞIMININ YORULMA ÇATLAĞI İLERLEME DAVRANIŞI

VARLI, Aziz Egemen

Yüksek Lisans, Metalurji ve Malzeme Mühendisliği Bölümü

Tez Yöneticisi Prof. Dr. Rıza GÜRBÜZ

Haziran 2006, 84 sayfa

AA6013 alüminyum alaşımında farklı yaşlandırma ısı işlemlerinin, yorulma çatlakları ilerleme davranışına olan etkisi incelenmiştir. L-T ve T-L doğrultularında K(Ç) (kompak çekme) numuneleri hazırlanmış ve bunlara yorulma çatlakları ilerleme hızı testleri yapılmıştır. Numuneler temin edildiği T651 halinde, 538 °C'de 90 dakika çözelti ısı işlemi yapılmış, suya verilmiş ve 96 saat oda sıcaklığında doğal olarak yaşlandırılmış T42 durumunda ve T42 işlemi üzerine 245 °C'de 12 saat yaşlandırılmış durumdadır. Isıl işlemlerden sonra tüm koşullar için sertlik ve iletkenlik ölçümleri yapılmıştır.

Yorulma çatlakları ilerleme testleri ilk temin edildiği ısı işlem durumu olan T651, T42 ve 245 °C'de yaşlandırılmış numunelere, laboratuvar ortamında gerilim oranı $R=0.1$ 'de ve 1 Hz frekansında sinüzoidal yük dalgasında gerçekleştirilmiştir. En yüksek yorulma çatlakları ilerleme direnci T651 durumunda T-L yönünde ve 245 °C'de 12 saat yaşlandırılmış durumda L-T durumunda gözlenmiştir.

Anahtar kelimeler: Yorulma çatlakları ilerleme hızı, kompakt çekme, çatlak uzunluğu, gerilme yoğunluğu genişliği, AA6013, yaşlanma.

This thesis is dedicated to my parents Raziye and Galip Varlı.

ACKNOWLEDGEMENTS

First and foremost, I would like to express a great deal of thanks and gratitude to Prof. Dr. Rıza Gürbüz for his encouragement, insight and close guidance. Prof. Gürbüz far exceeded my expectations from an advisor and made my entire graduate experience unforgettable.

Special thanks need to be given to my colleague Burak Durak, he patiently taught me the principles of data acquisition without which this thesis come true.

I would also take the opportunity to thank all my colleagues in TÜBİTAK-SAGE, Metallic and Ceramic Materials Division, for their help and invaluable discussing during my study.

Sincere thanks go to the following persons for their very helpful technical assistance, in particular to Şaban Seyhan and Ömer Akçay who always provided extra care to soldering and I must express my special thanks to Gül Çevik and Yaşar Kazanç for their helps during lab works.

TABLE OF CONTENTS

ABSTRACT	iv
ÖZ	v
ACKNOWLEDGEMENTS	vii
TABLE OF CONTENTS	viii
LIST OF TABLES	x
LIST OF FIGURES	xi
CHAPTERS	
1.INTRODUCTION	1
2.THEORY	3
2.1. Mechanism of Fatigue Crack Growth.....	3
2.2. Fatigue Crack Growth Rate	9
2.3. Crack Propagation Laws	11
2.4. AA6013 (Al-Mg-Si-Cu) Alloy	15
2.5. Heat Treatment of Aluminum Alloys	17
3.EXPERIMENTAL PROCEDURE	20
3.1. Material	20
3.2. Heat Treatment	21
3.3. Mechanical Tests	23
3.4. Metallography.....	23
3.5. The Specimens.....	25
3.6. Test Equipment.....	28
3.7. Testing and Data Acquisition	29

4.RESULTS AND DISCUSSION	36
4.1. Natural Aging and Overaging Heat Treatments	36
4.2. Metallographic Examination	39
4.3. Mechanical Properties.....	43
4.4. Determination of Stress Intensity Range.....	45
4.5. Crack Length vs. Number of Cycle Curves	46
4.6. Crack Growth Rate vs. Stress Intensity Range Plots	49
4.7. Application of Paris-Erdogan Law	56
4.8. Comparison of the da/dN vs. ΔK Plots	57
4.9. Macro Photographs of the Fracture Surfaces	64
4.10. Fractographic Analysis.....	66
5.CONCLUSIONS	81
REFERENCES	82

LIST OF TABLES

Table 4.1. Hardness and conductivity values for three different heat treatment conditions.	39
Table 4.2. Tensile properties of AA6013 in different for different heat treatment conditions and orientations.....	43
Table 4.3. Plain strain fracture toughness values of AA6013 under different conditions.	44
Table 4.4. Maximum stress intensity range, K_{\max}	45
Table 4.5. Paris-Erdogan constants.....	56
Table 4.6. Fatigue crack growth rate, da/dN (mm/cycle), values of T651, T42 and TOA conditions at $\Delta K = 20 \text{ MPa}\cdot\text{m}^{1/2}$	64
Table 4.7. Concentration table of EDS analysis of particle in Figure 4.25(a). ...	79
Table 4.8. Concentration table of EDS analysis of particle in Figure 4.30(b). ...	80

LIST OF FIGURES

Figure 2.1. Aloha Airlines Boeing 737-297, registration N73711, operating flight AQ243 from Hilo to Honolulu at Kahului Airport on April 28, 1988 after its fuselage was torn away during flight [4].....	4
Figure 2.2. The stage I and stage II crack growth processes in a polycrystalline material.....	6
Figure 2.3. Schematic of the slip band formation in a single grain. The external loadings acting vertically, in tension-compression cycling. The stage I and stage II crack growth processes in a polycrystalline material [6].	7
Figure 2.4. Neumann's model of crack nucleation [9].....	8
Figure 2.5. Plastic blunting process for growth of stage II fatigue crack [10].....	9
Figure 2.6. Schematic fatigue crack growth curve, crack length (a) vs. number of cycle (N) [6].	10
Figure 2.7. Three loading modes of a crack [6].....	12
Figure 2.8. Fatigue crack growth regimes, $\log da/dN$ versus $\log \Delta K$ [6].	13
Figure 2.9. Alternative Fuselage constructions [20].....	17
Figure 3.1. a) Air Furnace, b) Water quenching tank.	22
Figure 3.2. a) Hardness tester, b) Hocking™ Autosigma 3000 conductivity measurement device.....	22
Figure 3.3. Metallographic specimen preparation tools a) Table top cut-off machine b) Hot mounting press c) Grinding and polishing device.	24
Figure 3.4. Axioskop Mat 2 image analyze system located at TÜBİTAK-SAGE.	24
Figure 3.5. Compact Specimen, C(T) Standard Proportions and Tolerances [27].	25
Figure 3.6. Standard Compact-Tension C(T) Specimen for Fatigue Crack Growth Rate [29].....	26
Figure 3.7. Crack Starter Notch [27].	27

Figure 3.8. Orientation codes for rectangular sections according to ASTM E 399-90 [27].	27
Figure 3.9. MTS 810 universal testing machine with data acquisition system.	28
Figure 3.10. a) Assembled specimen b) Fracture moment.	29
Figure 3.11. Different types of crack foils.	31
Figure 3.12. Picture of gluing tool.	32
Figure 3.13. a) Picture of soldering operation, b) Prepared specimen.	32
Figure 3.14. Simplified scheme of gage circuit.	33
Figure 3.15. Screen shot of Daqview data acquisition software.	34
Figure 3.16. Scheme of test set-up.	35
Figure 4.1. Hardness Profile of AA6013 T42 alloy during aging at 245 °C.	37
Figure 4.2. Conductivity change of AA6013 T42 alloy during aging at 245 °C.	37
Figure 4.3. Micrograph of T651 condition a) in longitudinal b) in transverse.	40
Figure 4.4. Micrograph of T42 condition a) in longitudinal b) in transverse.	41
Figure 4.5. Micrograph of TOA condition a) in longitudinal b) in transverse.	42
Figure 4.6. Crack length vs. number of cycle curves for T651 L-T and T651 T-L.	46
Figure 4.7. Crack length vs. number of cycle curves for T42 L-T and T42 T-L.	47
Figure 4.8. Crack length vs. number of cycle curves for TOA L-T and TOA T-L.	47
Figure 4.9. Crack length vs. number of cycle curves for all conditions in L-T direction.	48
Figure 4.10. Crack length vs. number of cycle curves for all conditions in T-L direction.	48
Figure 4.11. da/dN vs. ΔK plot of T651 T-L.	50
Figure 4.12. da/dN vs. ΔK plot of T651 L-T.	51
Figure 4.13. da/dN vs. ΔK plot of T42 T-L.	52
Figure 4.14. da/dN vs. ΔK plot of T42 L-T.	53
Figure 4.15. da/dN vs. ΔK plot of TOA T-L.	54
Figure 4.16. da/dN vs. ΔK plot of TOA L-T.	55
Figure 4.17. da/dN vs. ΔK plot of T651 condition in two orientations.	58

Figure 4.18. da/dN vs. ΔK plot of T42 condition in two orientations.	59
Figure 4.19. da/dN vs. ΔK plot of overaged condition in two orientations.	60
Figure 4.20. da/dN vs. ΔK plots of T651, T42 and TOA condition in T-L orientation.....	61
Figure 4.21. da/dN vs. ΔK plots of T651, T42 and TOA condition in L-T orientation.....	62
Figure 4.22. From left to right, fracture surfaces of the T651 T-L and L-T specimens.	65
Figure 4.23. From left to right, fracture surfaces of the T42 T-L and L-T specimens.	65
Figure 4.24. From left to right, fracture surfaces of the TOA T-L and L-T specimens.	65
Figure 4.25. SEM photographs of T651 T-L specimen.	67
Figure 4.26. SEM Photographs of T651 T-L specimen.	68
Figure 4.27. SEM Photographs of T651 T-L specimen.	69
Figure 4.28. SEM photographs of T42 L-T specimen.	70
Figure 4.29. SEM photographs of T42 L-T specimen.	71
Figure 4.30. SEM photographs of T42 L-T specimen.	72
Figure 4.31. SEM photographs of T42 T-L	73
Figure 4.32. SEM photographs of TOA T-L specimen.	74
Figure 4.33. SEM photographs of different specimens.	75
Figure 4.34. SEM photographs of TOA L-T specimen.	76
Figure 4.35. SEM photographs of TOA L-T specimen.	77
Figure 4.36. EDS analysis of particle in Figure 4.25(a).	79
Figure 4.37. EDS analysis of particle in Figure 4.30(b).	80

CHAPTER 1

INTRODUCTION

Aluminum is the second most plentiful metallic element on earth. Although pure aluminum is too soft and weak for structural applications, the strength of aluminum alloys can be greatly improved by a process called age or precipitation hardening. Those heat-treatable aluminum alloys have been widely used in the automobile and aerospace industries because of their superior strength to weight ratios.

Alloy 6013 is a member of the family of age hardenable Al-Mg-Si-(Cu) alloys (Al-6xxx series), which, due to the high yield strength that can be achieved, are used in aerospace applications for structural components. The yield strength levels need to be kept as high as possible, cause the application is strength dominated. On the other hand, fracture toughness and corrosion resistance are also important properties, since the structures that this product is used must resist fracture and exhibit resistance to aggressive aqueous environments. Increasing the fatigue resistance is an interesting technological challenge and becomes important from a performance standpoint.

To better design structures and machines, understanding of flaws and failures is essential. Failure by high cycle fatigue is evolves three distinct regimes: crack initiation, crack growth and fracture. A large portion of the service life of aerospace products elapses during the crack initiation and crack growth regions of the total fatigue life of a component. The body of this work addresses the determination of fatigue crack growth behavior of AA6013 alloy at different heat treatment conditions.

The heat treatment of alloy AA6013 has been achieved for three conditions and fatigue crack growth behaviour was investigated in transverse-longitudinal (T-L) and longitudinal-transverse (L-T) directions. Material has been purchased at peak aged condition, T651 and two other heat treatments have been achieved. T42 condition was achieved by solution heat treating of original alloy followed by natural aging at room temperature for 96 hours. Finally a heat treatment is achieved over T42 condition by artificially aging at 245 °C for 12 hours. Fatigue crack growth tests were performed at laboratory air condition.

CHAPTER 2

THEORY

2.1. Mechanism of Fatigue Crack Growth

The discovery of fatigue occurred in the 1800s when several investigators in Europe observed that bridge and railroad components were cracking when subjected to repeated loading [1]. As the century progressed and the use of metals expanded with the increasing use of machines, more and more failures of components subjected to repeated loads were recorded.

Fatigue is defined as a term which applies to changes in properties which can occur in a metallic material due to the repeated application of stresses or strains, although usually this term applies specially to those changes which lead to cracking or failure [2]. The vast majority of practical engineering design applications involve fluctuating or cyclic loads well below the yield stress of the material of interest. Despite the low magnitude of these stresses, damage can accumulate and “fatigue failure” can occur. It is estimated that over 80 percent of all brittle fractures involve some period of fatigue crack growth [3].

There is little doubt that fatigue plays a significant role in all industrial design applications. Many components are subjected to some form of fluctuating stress/strain, and thus fatigue potentially plays a role in all such cases. However, it is still vital that all designs consider those aspects of nucleation processes other than fatigue that may act to nucleate cracks that could propagate under the influence of cyclic loads. The intrinsic state of the material and all potential sources of cracks must also be evaluated. Figure 2.1 shows a fatal fatigue failure.

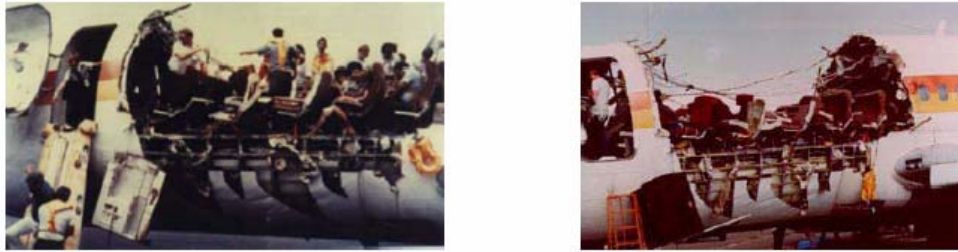


Figure 2.1. Aloha Airlines Boeing 737-297, registration N73711, operating flight AQ243 from Hilo to Honolulu at Kahului Airport on April 28, 1988 after its fuselage was torn away during flight [4].

Fatigue may conclude into cracks and cause fracture after a sufficient number of fluctuations. Fatigue damage is caused by the simultaneous action of cyclic stress, tensile stress, and plastic strain. If any one of these three is not present, a fatigue crack will not initiate and propagate. The plastic strain resulting from cyclic stress initiates the crack; the tensile stress promotes crack growth (propagation). Although compressive stresses will not cause fatigue, compressive loads may result in local tensile stresses. Microscopic plastic strains also can be present at low levels of stress where the strain might otherwise appear to be totally elastic [5].

Fatigue cracks generally initiate in a highly stressed region of a component subjected to cyclic stresses of sufficient magnitude. The crack propagates under the applied stress through the material until complete fracture results. On the microscopic scale, the most important feature of the fatigue process is the nucleation of one or more cracks under the influence of reversed stresses that exceed the flow stress, followed by the development of cracks at persistent slip bands or at grain boundaries. Subsequently, fatigue cracks propagate by a series

of opening and closing motions at the tip of the crack that produce, within the grains, striations that are parallel to the crack front [6].

The process of fatigue consists of three stages:

Stage I: Initial fatigue damage leading to crack nucleation and crack initiation.

Stage II: Crack propagation until the remaining uncracked cross section of a part becomes too weak to sustain the loads imposed.

Stage III: Final, sudden fracture of the remaining cross-section.

When the crack and the zone of plastic deformation surrounding the crack tip are confined to within a few grain diameters, crack growth occurs mostly by single shear, in the direction of the primary slip system. This single slip mechanism leading to a crack whose length values substantially larger than the grain size provided that the zone of near-tip plasticity is smaller than the grain dimensions. At higher stress intensity range values, the plastic zone at the crack tip encompasses many grains. The attendant crack growth process involves simultaneous or alternating flow along two slip systems. This duplex slip mechanism, termed stage II, results in a planar crack path normal to the far field tensile axis [7]. First two stages mechanisms are illustrated in Figure 2.2.

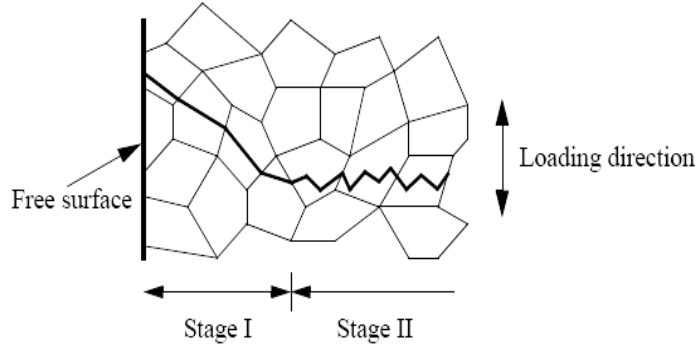


Figure 2.2. The stage I and stage II crack growth processes in a polycrystalline material.

The nucleation process for undamaged materials can be described by the intrusion-extrusion mechanism, shown in Figure 2.3. Slip bands are formed as a result of dislocation movement within individual grains. Each grain will have a different preferred slip plane depending on the crystal structure. At low stresses, only a few grains have favorable orientations, where the shear stresses are high enough to initiate plastic deformation, and only a few slip bands form. At high stresses, plastic deformation occurs in many grains, and a large number of slip bands form. During repeated cyclic loading, the slip is working back and fourth on the slip bands and eventually a fatigue crack is formed along the persistent slip band. An important structural feature, which appears to be unique to fatigue deformation, is the formation on the surface of ridges and grooves called slip-band extrusions and slip-band intrusions. Extremely careful metallography on narrowed sections through the surface of the specimen has shown that fatigue cracks initiate at intrusions and extrusions [8].

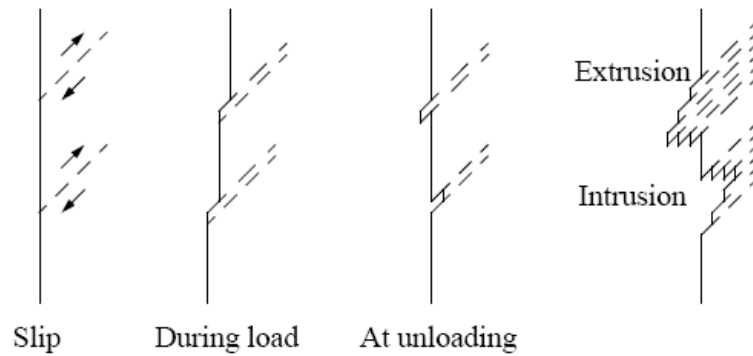


Figure 2.3. Schematic of the slip band formation in a single grain. The external loadings acting vertically, in tension-compression cycling. The stage I and stage II crack growth processes in a polycrystalline material [6].

Neumann [9] proposed a model for the formation of cracks by coarse slip on alternating parallel slip planes (Figure 2.4.). In this model, the crack develops from coarse slip steps. In tension (Figure 2.4. (a)), slip plane 1 is activated; excess dislocations of one sign remain on this slip plane. The slip step that is produced acts as a stress raiser, which also helps to activate slip plane 2 under the same tensile load. This leads to the configuration shown in Figure 2.4(b) and to excess dislocations of one sign on plane 2. During the next compression, excess dislocations on slip planes 1 and 2 run back, leading to the configuration shown in Figure 2.4(c). It is assumed that at A in Figure 2.4(c) the surfaces are not rewelded but rather only touch macroscopically. Thus, A in Figure 2.4(c) already represents a crack nucleus. Repetition of this process takes place on further glide planes of the same slip systems, leading to continuous increase of microcrack length. Note that in this model, the crack nucleation is on an average plane, which is perpendicular to the maximum tensile stress as opposed to parallel to the shear plane as in the case of intrusion formation.

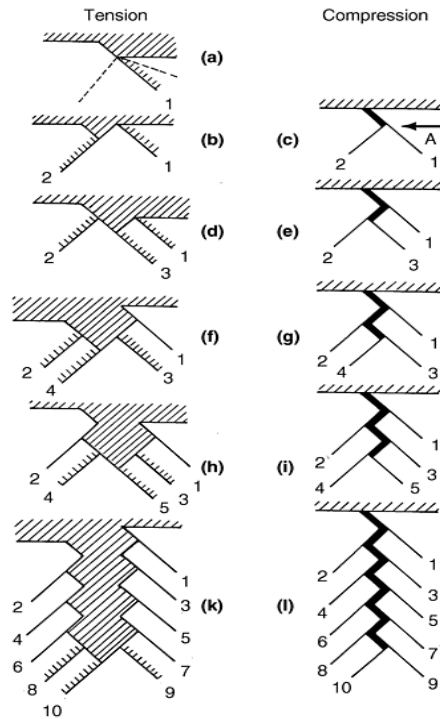


Figure 2.4. Neumann's model of crack nucleation. [9].

Stage II crack propagation occurs by a plastic blunting process that is illustrated in Figure 2.5. At the start of loading cycle, the crack tip is sharp (Figure 2.5(a)). As the tensile load is applied, the small double notch at the crack tip concentrates the slip along planes 45° to the plane of the crack (Figure 2.5(b)). As the crack widens to its maximum extension (Figure 2.5(c)) it grows longer by plastic shearing and at the same time, its tip becomes blunter. When the load is changed to compression the slip direction in the end zones is reversed (Figure 2.5d). the crack faces are crushed together and the new crack surface created in tension is forced into the plane of the crack (Figure 2.5(e)) where it partly folds by buckling to form a resharpened crack is then ready to advance and be blunted in the next stress cycle [10].

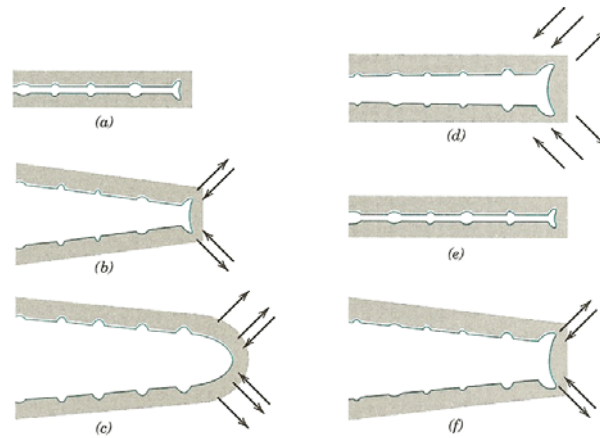


Figure 2.5. Plastic blunting process for growth of stage II fatigue crack [10].

2.2. Fatigue Crack Growth Rate

The majority of fatigue life may be taken up in the propagation of a crack. By the use of fracture mechanics principles it is possible to predict the number of cycles spent in growing a crack to some specified length or to final failure. The aircraft industry has been instrumental in the effort of to understand and predict fatigue crack growth. They have developed the safe-life or fail-safe design approach. In this method, a component is designed such that if a crack forms, it will not grow to a critical size between specified inspection intervals. Thus, by knowing the material growth rate characteristics and with regular inspections, cracked component may be kept in service for an extended useful life [11].

Fatigue crack growth rate can be defined basically by the crack growth, da , with the number of cycle, dN , and implied by the ratio da/dN , which is also equal to the slope of the crack growth curve shown in Figure 2.6.

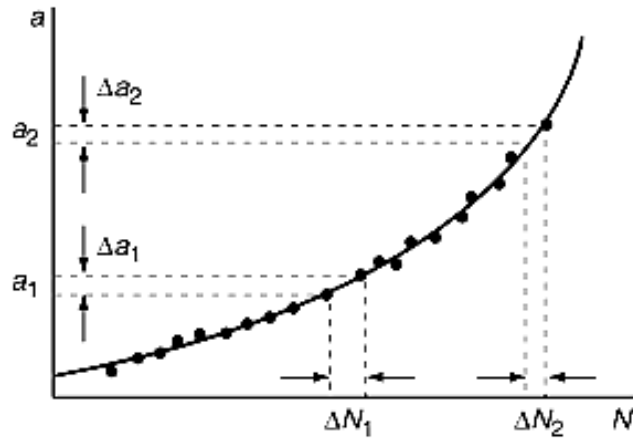


Figure 2.6. Schematic fatigue crack growth curve, crack length (a) vs. number of cycle (N) [6].

When a component or a specimen containing a crack is subjected to cyclic loading, the crack length (a) increases with the number of fatigue cycles, N , if the load amplitude (P), load ratio (R), and cyclic frequency (ν), are held constant. The crack growth rate, da/dN , increases as the crack length increases during a given test. The da/dN is also higher at any given crack length for tests conducted at higher load amplitudes [6]. From a philosophical standpoint, a stress can never be applied, but a load can. Stress is always a resultant and determined quantity; it is not measurable. It is a mathematical device that has some very useful characteristics and provides a wealth of interpretations and insights, especially in reflecting an area rationalized force (load) path through the structure. Structures and materials, however, only experience loads (mechanical, thermal, chemical, etc.) and respond with strains and displacements. Thus, the following functional relationship can be derived from these observations:

$$\left(\frac{da}{dN} \right)_{R,\nu} = f(\Delta P, a) \quad (2.1)$$

Where the function f is dependent on the geometry of the specimen, the crack length, the loading configuration, and the cyclic load range. This general relation is simplified with the use of the stress intensity range parameter, ΔK as defined below.

$$\Delta K = K_{\max} - K_{\min} \quad (2.2)$$

$$K_{\max} = f(\sigma_{\max}, a) \quad (2.3)$$

$$K_{\min} = f(\sigma_{\min}, a) \quad (2.4)$$

Stress intensity range can also be expressed in terms of stress ratio by the following relationships:

$$\Delta K = (1 - R)K_{\max} \quad \text{for } R \geq 0 \quad (2.5)$$

$$\Delta K = K_{\max} \quad \text{for } R \leq 0 \quad (2.6)$$

$$R = \frac{\sigma_{\min}}{\sigma_{\max}} = \frac{K_{\min}}{K_{\max}} \quad (2.7)$$

As it seen from the Equation 2.5 above, ΔK is equal to K_{\max} when minimum stress is compressive or zero. The stress ratio, R , can also be written as the K_{\min} to K_{\max} ratio [6].

2.3. Crack Propagation Laws

In 1963, Paris and Erdogan [12] published an analysis consisting of considerable fatigue crack growth rate (FCGR) data and demonstrated that a correlation exists between da/dN and the cyclic stress intensity parameter, ΔK . They argued that ΔK characterizes the magnitude of the fatigue stresses in the crack-tip region; hence, it should characterize the crack growth rate. Such a proposition is in obvious agreement with the functional relationships of. The parameter ΔK accounts for the magnitude of the load range (ΔP) as well as the crack length and

geometry. A number of later studies have confirmed the findings of Paris and Erdogan. The data for intermediate FCGR values can be represented by the following simple mathematical relationship, commonly known as the Paris equation:

$$\frac{da}{dN} = C\Delta K^m \quad (2.8)$$

Where C and m are constants that can be obtained from the intercept and slope, respectively, of the linear log (da/dN) versus log (ΔK) plot. This representation of FCGR is a useful model for midrange FCGR values.

The exponent m is typically between two and four for ductile metallic alloys [13]. For tensile fatigue, it is understood that ΔK refers to the range of mode I stress intensity factors during the stress cycle. Similarly, a stress intensity factor range ΔK_{II} and ΔK_{III} can also be used in Paris-Erdogan law to characterize fatigue crack growth in mode II and mode III respectively.

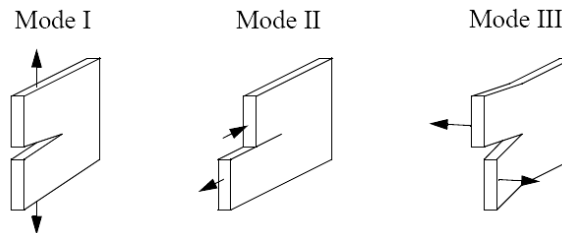


Figure 2.7. Three loading modes of a crack [6].

Fatigue crack propagation data obtained from a laboratory can be divided into three regions as seen in Figure 2.8. Region I is typically referred to as the

threshold regime and is composed of slow crack growth behavior. Region II is sometimes called the Paris regime in recognition of P.C. Paris as the researcher who first correlated stress intensity factor range with fatigue crack growth rate. The mentioned correlation is a linear one in log-log coordinates. The final region is one in which the maximum stress intensity factor K_{\max} approaches the fracture toughness K_{IC} and is composed of rapid crack growth. The axes in Figure 2.8 are da/dN and ΔK the fatigue crack growth rate and stress intensity factor range respectively.

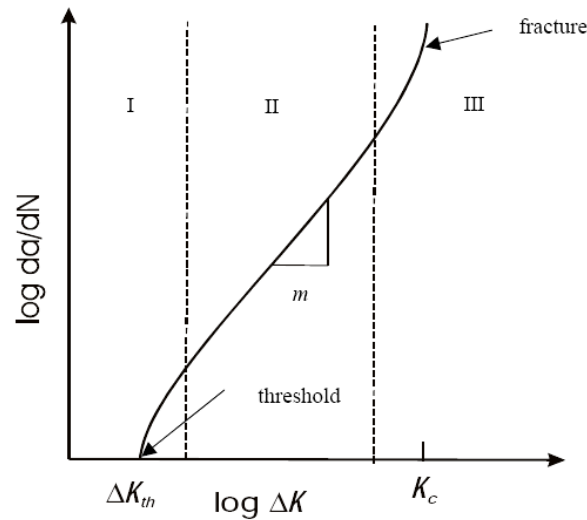


Figure 2.8. Fatigue crack growth regimes, $\log da/dN$ versus $\log \Delta K$ [6].

The Paris equation accurately represents the behavior of many materials in the mid- ΔK range, which is of significant engineering interest. This equation does not recognize the effects of load ratio (P_{\min} / P_{\max}), the existence of a threshold

ΔK_{th} , or very high acceleration of the fatigue crack propagation (FCP) rate as the stress intensity approaches the fracture toughness of the material [12].

Another simple equation, known as the Forman equation, has found wide application in correlating FCP data for aluminum alloys [14].

$$\frac{da}{dN} = \frac{C\Delta K^m}{(1-R)K_c - \Delta K} \quad (2.9)$$

Where C and m are material specific constants different from the Paris coefficients and $K_c \approx K_{Ic}$. Similar to the Forman's equation Walker [15] developed another correlation which is shown below.

$$\frac{da}{dN} = \frac{C\Delta K^m}{(1-R)^{m(1-\gamma)}} \quad (2.10)$$

Once again, the constant coefficients C and m are not related to the previous expressions and the γ term adjusts for R effects. Of the two previous expressions, the addition of stress ratio R into the equations is of considerable significance. Research has shown that da/dN vs. ΔK data for a single material varies with stress ratio R. Due to this dependence; a plot of da/dN vs. ΔK cannot truly be considered a material property.

It must be emphasized that the real utility of these representations lies in data correlation and life calculations. It is not possible to use such equations to gain insight into the mechanisms associated with the FCP process or to design new alloys for increased fatigue resistance.

In 1973, Pearson [16] drew attention to the fact that short fatigue cracks could grow at stress intensity levels below the threshold level for macroscopic cracks.

$$\frac{da}{dN} = \frac{C\Delta K^m}{[(1-R)K_c - \Delta K]^{1/2}} \quad (2.11)$$

Ewalds and Wanhill [17] propose a formula to describe sigmoidal morphology by the formula below.

$$\frac{da}{dN} = C\Delta K^m \left[\frac{1 - \left(\frac{\Delta K_{th}}{\Delta K}\right)^{n_1}}{1 - \left(\frac{\Delta K_{max}}{\Delta K}\right)^{n_2}} \right]^{n_3} \quad (2.12)$$

Where ΔK_{th} is the near threshold intensity factor and n_1 , n_2 and n_3 are empirically determined exponents.

2.4. AA6013 (Al-Mg-Si-Cu) Alloy

Weight savings are the everyday challenges of the structural designers and materials specialists, whereas cost reduction is the daily request of the procurement and manufacturing departments. As aerospace industry develops, new aluminum alloys for aircraft structures have been designed to improve the weight efficiency of the structures where alloy AA6013 is one of them.

Alloy 6013 is a new medium strength aerospace alloy that provides improved corrosion resistance and formability for use in aerospace applications including primary aircraft structures. Alloy 6013 is an aluminum-magnesium-silicon-copper alloy that has yield strengths 12% higher than that of alclad 2024-T3 and is virtually resistant to exfoliation and stress corrosion cracking. Industry use has demonstrated that alloy 6013 in the T4 condition has better stretch forming characteristics than other aerospace aluminum alloys. Parts can be formed in the T4 condition and aged to the T6 condition without costly heat treatment or annealing operations [18].

Uses for AA6013 comprise primary structural applications including fuselage panels, leading and trailing edges and engine cowlings. Lockheed has chosen AA6013-T6 for the fuselage of the Navy's P-7A aircraft. Canadair has specified AA6013-T6 for the leading edges of the Regional Jet [18].

Alloy 6013 is receiving consideration in most new programs taking advantage of the improved formability, lower density, and corrosion resistance. AA6013 is weldable with both MIG and TIG welding methods. Tests show that AA6013 does not weld crack with 4XXX series (4043, 4643, etc.) filler alloys [18].

Until a couple of years ago mainly the standard skin sheet alloy AA2024 (Al-Cu-Mg) was used for joining of fuselage structures by riveting or bonding. Since the advanced Laser Beam Welding (LBW) joining technique results in higher weight and cost savings than riveting or bonding, two years ago the first LBW fuselage shells were implemented in the Airbus aircraft A318. For realization of such LBW structures, weldable Al alloys have to be used. However, alloy AA2024 is non-weldable. One suitable choice for LBW is the alloy AA6013, which has similar mechanical properties to AA2024 under laboratory conditions [19].

The 6XXX alloys have been considered to replace 2024 on a number of US Navy programs and alloy 6013 is being used on the Boeing 777. The major problem with 2XXX alloys for fuselage skins is that they must be clad since they can be susceptible to intergranular corrosion. In addition, the 2XXX alloys cannot be fusion welded, a process that is being considered for reducing weight and costs of manufacturing. The 6XXX alloys are weldable and cheaper than 2XXX alloys, however, Cu-rich 6XXX, e.g. 6013-T6 and 6056-T6 are also susceptible to intergranular corrosion. This susceptibility is associated with the formation of precipitate free zones at grain boundaries, which are developed during artificial aging, are depleted in Si and Cu, and are anodic with respect to the grains [19].

Opportunity corresponds to the use of new weldable aluminum alloys, possibly associated with extruded panels, to replace riveted assemblies by welded structures [20], see Figure 2.9.

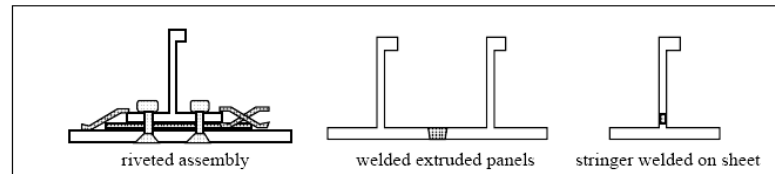


Figure 2.9. Alternative Fuselage constructions [20].

2.5. Heat Treatment of Aluminum Alloys

Heat treating in its broadest sense, refers to any of the heating and cooling operations that are performed for changing the mechanical properties, the metallurgical structure, or the residual stress state of a metal product. When the term is applied to aluminum alloys, however, its use frequently is restricted to the specific operations employed to increase strength and hardness of the precipitation-hardenable wrought and cast alloys. These usually are referred to as the "heat-treatable" alloys to distinguish them from those alloys in which no significant strengthening can be achieved by heating and cooling. The latter, generally referred to as "non- heat-treatable" alloys, depend primarily on cold work to increase strength. Heating to decrease strength and increase ductility (annealing) is used with alloys of both types; metallurgical reactions may vary with type alloy and with degree of softening desired [21].

In designing alloys for strength, an approach often taken is to develop an alloy in which the structure consists of particles, which obstruct dislocation motion dispersed in a ductile matrix. The finer the dispersion, for the same amount of particles, the stronger the material. These finer dispersions can only be achieved by age hardening in aluminum alloys. Age hardening in aluminum was discovered by chance in 1906 [19]. This effect is vital for the application of the lightweight metal aluminum for aircraft structures.

Heat treatment to increase strength of aluminum alloys is a three-step process:

- Solution heat treatment: dissolution of soluble phases.
- Quenching: development of supersaturation.
- Age hardening: precipitation of solute atoms either at room temperature (natural aging) or at elevated temperature (artificial aging or precipitation heat treatment).

The general requirement for precipitation strengthening of supersaturated solid solutions involves the formation of finely dispersed precipitates during aging heat treatments (which may include either natural aging or artificial aging). The aging must be accomplished not only below the equilibrium solvus temperature, but also below a metastable miscibility gap called the Guinier-Preston (GP) zone solvus line. The supersaturation of vacancies allows diffusion, and thus zone formation, to occur much faster than expected from equilibrium diffusion coefficients. In the precipitation process, the saturated solid solution first develops solute clusters, which then become involved in the formation of transitional (nonequilibrium) precipitates.

There are two main precipitate formation mechanisms for the alloy 6013 which are shown below.

Super Saturated Solution → Guiner-Preston Zones → β' (Mg_2Si) → β (Mg_2Si)

Super Saturated Solution → Q ($\text{Al}_5\text{Cu}_2\text{Mg}_8\text{Si}_6$) [20]

According to Starke and Staley [22], there are also intermetallic constituent particles in Al alloys. These form by a liquid-solid eutectic reaction during solidification, primarily from iron and silicon impurities. Because the low solubility of iron in pure aluminum is reduced by alloying elements, constituent particles containing iron are insoluble. Although silicon has appreciable solubility in aluminum, its solubility decreased by alloying elements, particularly magnesium. The size and size distribution of insoluble constituent particles are controlled by the rate of ingot solidification, the chemical composition, the extend and nature of bulk deformation. Particle size decreases as solidification rate increases. Generally, the insoluble constituent particles are coarsest and most heterogeneously distributed in thick plate and are finer and more homogeneously distributed in thin sheet. The constituent phase of AA6013 is $\text{Al}_{12}(\text{Fe}, \text{Mn})_3\text{Si}$ [22].

CHAPTER 3

EXPERIMENTAL PROCEDURE

3.1 Material

The material used in this thesis study was a rolled aluminum alloy AA6013 Power Plate (registered trademark of Alcoa) with a thickness of 25.4 mm. Material was produced at the Alcoa Davenport Works, Pittsburgh, with a production lot number of 451661 and a package ticket number of 755624. It was produced according to the ASTM B 209-04 [23] standard, which covers the properties of aluminum and aluminum alloy flat sheet, coiled sheet, and plate products.

The chemical composition limits and the actual composition of the alloy AA6013, in weight percentages are given in the Table 3.1.

Table 3.1. The chemical composition of AA6013 in weight percentages.

	Si	Fe	Cu	Mn	Mg	Cr	Zn	Ti	Other Each	Other Total	Al
Max.	1.00	0.50	1.10	0.80	1.20	0.10	0.25	0.10	0.05	0.15	Remain
Min.	0.60	-	0.60	0.20	0.80	-	-	-	-	-	
Actual	0.70	0.25	0.90	0.28	0.90	0.03	0.02	0.02	-	-	

3.2. Heat Treatment

The material was in T651 condition when it was purchased. Its original heat treatment condition was achieved at the Alcoa Davenport Works by solution heat treated at 538 °C, aged at room temperature for 96 hours and artificially aged at 191 °C for 4-5 hours. In addition, material was stress relieved by stretching after solution heat treatment or after cooling from an elevated-temperature shaping process to an amount of permanent set % 1.5-3.

In addition to the original heat treatment condition T651, two other heat treatments were also achieved to compare the fatigue crack growth behavior of the alloy in different conditions.

One of the other heat treatment conditions was T42 condition, which was first solution heat treated at 538 °C for 90 minutes and water quenched. After water quenching, material was naturally aged at room temperature for 96 hours.

Lastly, an overaged condition was achieved by aging the material at 245 °C for 12 hours after T42 heat treatment was applied. By this treatment an overaging condition was tried to be achieved, and this heat treatment condition is called as TOA in this thesis.

All the heat treatment processes were done according to SAE AMS 2770G standard [24] with using a convection air furnace, which has a temperature uniformity tolerance of ± 6 °C and equipped with a water quenching tank shown in Figure 3.1.



(a)



(b)

Figure 3.1. a) Air Furnace, b) Water quenching tank.

Hardness tests were conducted by using Mettest hardness measurement equipment, and conductivity measurements were performed with Hocking™ Autosigma 3000 (GE Inspection) conductivity measurement device, see Figure 3.2.



(a)



(b)

Figure 3.2. a) Hardness tester, b) Hocking™ Autosigma 3000 conductivity measurement device.

After the heat treatments materials were controlled in terms of their hardness and conductivity values, according to the SAE AMS 2658B [25] standard.

3.3. Mechanical Tests

The tensile strengths of the alloy AA6013 was obtained for different orientations and the heat treatment conditions. The values of T651 conditions were tested and certified by the ALCOA in the DS-700966-1 numbered certified inspection report. For the other conditions, tension tests were performed according to ASTM E 8M-04 [26].

The material was also tested to determine its plain strain fracture toughness values, for all conditions and directions. These tests were conducted according to the standard ASTM E 399-90 (Reapproved 1997) [27].

3.4. Metallography

After the heat treatments were completed, the microstructure of the alloy for all conditions all conditions was examined with metallographic techniques. Metallographic specimens were prepared starting with the cutting of the metallographic specimens with a tabletop cut-off machine. Following this, hot mounting took place. At the end, with grinding and polishing operations specimens became ready for etching. Specimens were grinded with 320, 500, 800, 1200 and 2400 grade grinding papers before polishing, and all specimens were polished with 1 μ m and 0.3 μ m alumina powder suspension. Figure 3.3 shows metallographic specimen preparation devices and tools that are used in this study.

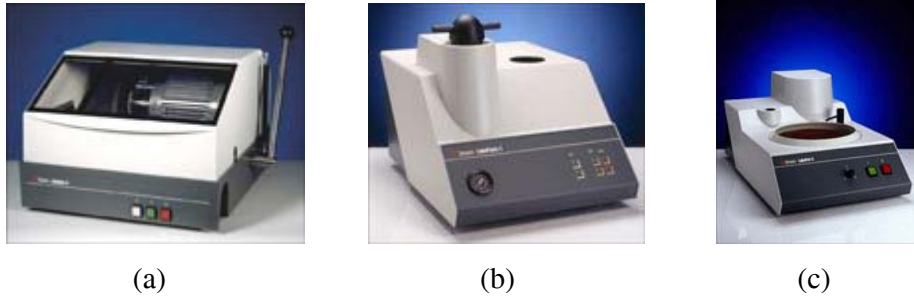


Figure 3.3. Metallographic specimen preparation tools a) Table top cut-off machine b) Hot mounting press c) Grinding and polishing device.

Following mechanical preparation of the specimens, before microscopic investigation, chemical preparation of the specimens was done. According to ASTM E 407-99 [28] to determine the general structure of the 6xxx series aluminum alloys etchant 3a, which has a composition of 2 ml HF, 3 ml HCl , 5 ml HNO₃ of and 190 ml of water, was preferred.

Specimens were examined under a Carl-Zeiss, Axioskop Mat 2 image analyzer system, Figure 3.4.



Figure 3.4. Axioskop Mat 2 image analyze system located at TÜBİTAK-SAGE.

3.5. The Specimens

In this study, the C(T) type specimens were prepared for both fatigue crack growth tests and fracture toughness (K_{Ic}) tests. Specimens were prepared from the plate with two different orientations designated as T-L and L-T. The C(T) type specimen's relative dimensions are shown in Figure 3.5 and Figure 3.6 for fracture toughness tests and fatigue crack growth rate tests, respectively.

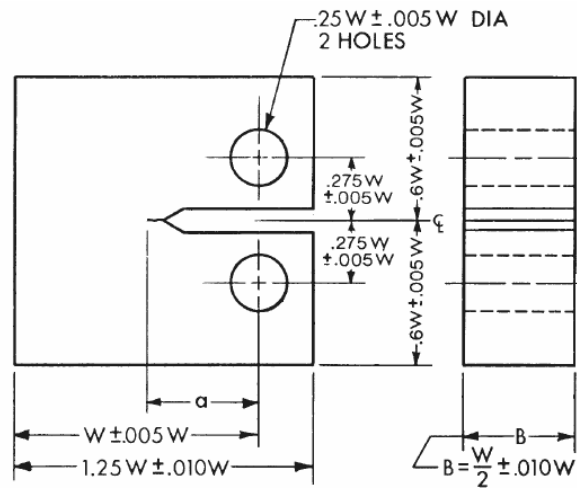


Figure 3.5. Compact Specimen, C(T) Standard Proportions and Tolerances [27].

For K_{Ic} test specimens, $W = 50$ mm and $B = 25$ mm were selected to calculate fracture toughness.

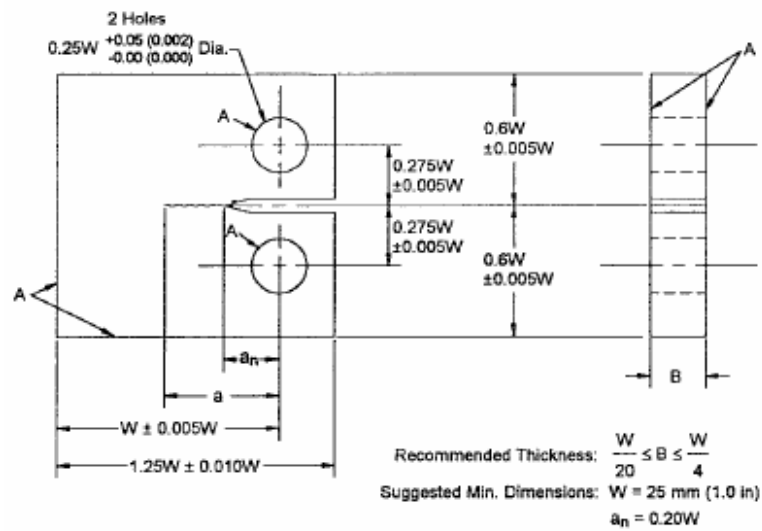


Figure 3.6. Standard Compact-Tension C(T) Specimen for Fatigue Crack Growth Rate [29].

In this thesis study, C(T) specimens were prepared with dimensions of $W=40 \text{ mm}$ and $B=10 \text{ mm}$. These sizes follow to the recommended thickness value relation of $W/20 \leq B \leq W/4$ in ASTM E 647-00 [29].

Both fracture toughness and fatigue crack growth rate tests were performed with chevron type notched specimens, see Figure 3.7. The orientation codes according to ASTM B 399-90 are shown in Figure 3.8.

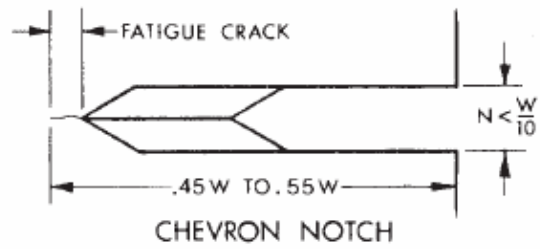


Figure 3.7. Crack Starter Notch [27].

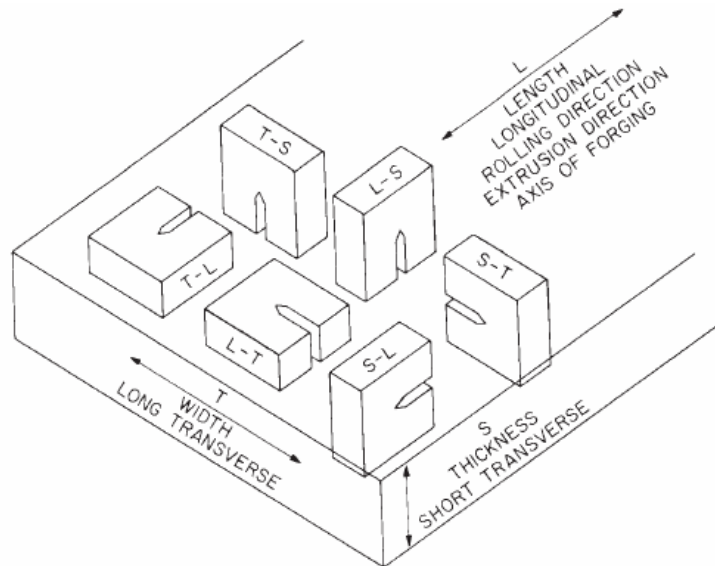


Figure 3.8. Orientation codes for rectangular sections according to ASTM E 399-90 [27].

3.6. Test Equipment

Fatigue crack growth rate tests and fatigue pre-cracking for fracture toughness tests were executed with MTS 810, servo-hydraulic universal test machine. Fracture toughness tests' final loadings, after pre-cracking, were performed with Aİşa tension-compression testing machine. In Figure 3.9 MTS 810 can be seen with the data acquisition system.



Figure 3.9. MTS 810 universal testing machine with data acquisition system.

During pre-cracking of the fracture toughness test specimens, crack growth measurement was conducted by using a traveling microscope with a resolution of ± 0.01 mm.

Crack growth measurements during fatigue crack growth tests were performed with a crack gage, which will be explained in detail in the next section.

3.7. Testing and Data Acquisition

The goal of this study was to investigate the effect of heat treatment and the orientation of loading on the fatigue crack growth behavior of AA6013 alloy. Accordingly, heat treatments were achieved and consequently specimens were machined. Heat treatments were peak aged T651, T42 naturally aged and an overaged condition as explained before.

A clevis and pin assembly (Figure 3.10) was used at both the top and bottom of the specimen to allow in-plane rotation as the specimen is loaded. All specimens were pre-cracked with a constant amplitude sinusoidal load at a frequency of 10 Hz. Fatigue pre-cracking was achieved until the sufficient crack length reached in conformity with ASTM E 647-00.

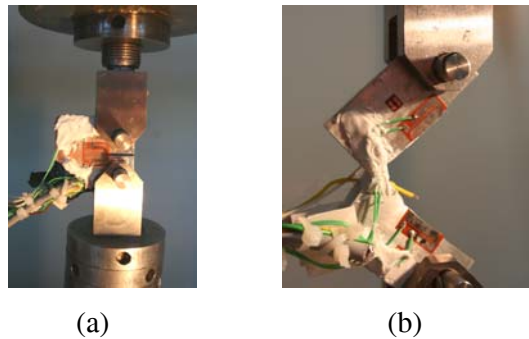


Figure 3.10. a) Assembled specimen b) Fracture moment.

Fatigue crack growth rate tests were performed in laboratory atmosphere and at room temperature. Constant amplitude tensile to tensile sinusoidal load waves were applied to the specimens with a frequency of 1 Hz. The stress ratio, R , was constant for all tests and it was 0.1.

Crack length measurement was achieved in this study by using a bonded foil crack gage system, with a trademark Krak-Gage™. Gages were purchased from Rumul, Russenberger Prüfmaschinen AG. Paris and Hayden [30] have reported that a bonded, metal foil-type gage [31] is a useful new addition to Fracture Mechanics Testing and Instrumentation. It was reported that this system was compatible with ASTM Standard E 647-81, the “Tentative Test Method for Constant-Load-Amplitude Fatigue Crack Growth Rates above 10^{-8} m/cycle” and easily exceeded the accuracy and sensitivity requirements of ASTM E 647-81. Liaw and Hartmann [32] showed that the Krak-Gage performed satisfactorily, and the test data compared favorably with comparative data obtained from other methods in laboratory atmosphere and in 100% relative humidity environments, respectively, for aluminum alloys and a steel.

This gage, or transducer, is a bondable, thin, electrically insulated metal foil of certain dimensions photo-etched from a constantan alloy. The gage backing is flexible epoxy-phenolic matrix providing the necessary insulation and bonding surface area similar to the technology of foil-type strain gages. Conventional, well-established foil strain-gage installation techniques are applied to the bonding and installation of such a gage to the test specimen. By an appropriate selection of gage material, gage size, backing and adhesive bonding a crack will simultaneously propagate in both the test specimen and the bonded Krak-Gage [32].

There are several gage dimensions for different specimen sizes. In this study A10 type gages were used, in Figure 3.11 different gage types are shown.

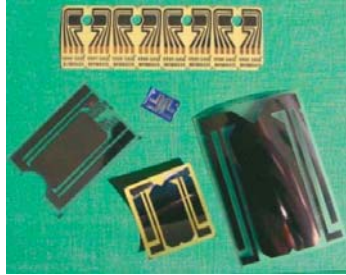


Figure 3.11. Different types of crack foils.

Crack detector foils were glued in such a manner that the foils fit the machined notch properly. For gluing the foils a two-component epoxy resin araldite adhesive was used. Resin and hardener were first mixed to the ratio of 1:1; specimen surfaces were cleaned with alcohol and followed by heating the specimens to 50 °C in a drying oven. Afterwards, the araldite was swelled thinly and evenly with the help of a pallet, lastly, crack detector foil was positioned and hand pressed on evenly by means of thin PVC foil. This operation was handled very carefully in order to prevent adhesive contamination on the top of the foil, which could cause difficulties during soldering operation. Once the positioning of the foil was achieved, a Teflon foil replaced PVC foil, and specimens were pressed under a gluing tool for 15 minutes. Gluing tool is shown in Figure 3.12.



Figure 3.12. Picture of gluing tool.

After gluing the foils to the specimens, a four-channel data transfer cable was installed by soldering. To prepare the specimens for soldering crack foils were cleaned with Trichloroethylene to remove the adhesive on the top side of the foils. In Figure 3.13, soldering operation and prepared specimen are shown.

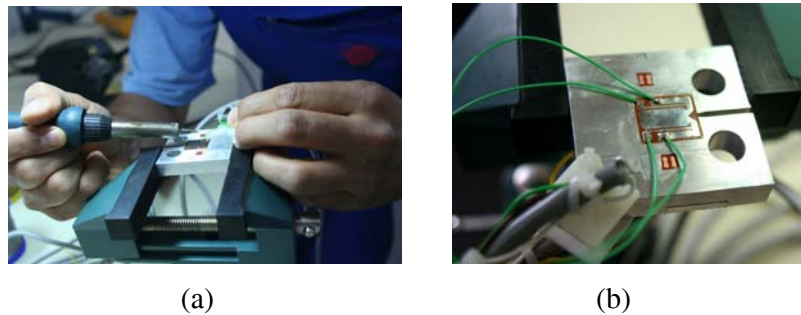


Figure 3.13. a) Picture of soldering operation, b) Prepared specimen.

The basic principle of the Krak-Gage employs an indirect D.C. potential measurement technique. A constant current source was used to excite the low

resistance crack gage. A propagating crack produces a large change in the resistance of the gage and yields a high D.C. output, proportional to crack length, of 0-100 mV for the full-scale rating of the gage. In Figure 3.14, simplified circuit of the gage is shown.

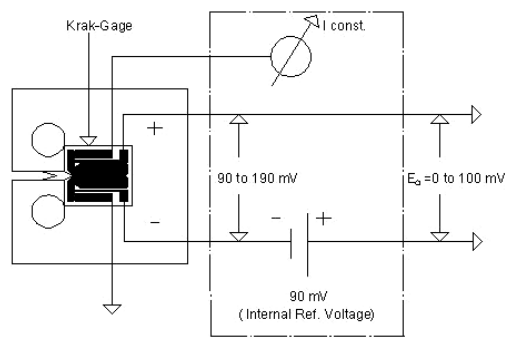


Figure 3.14. Simplified scheme of gage circuit.

The output voltage (ΔV) of the Krak-Gage was read by using a IOTECH DaqBoard/500™ PCI analog to digital (a/d) converter card and a software named Daqview™ which was installed to a computer. A screen shot picture of Daqview software is shown in Figure 3.15. The test set of connections are shown in Figure 3.16.

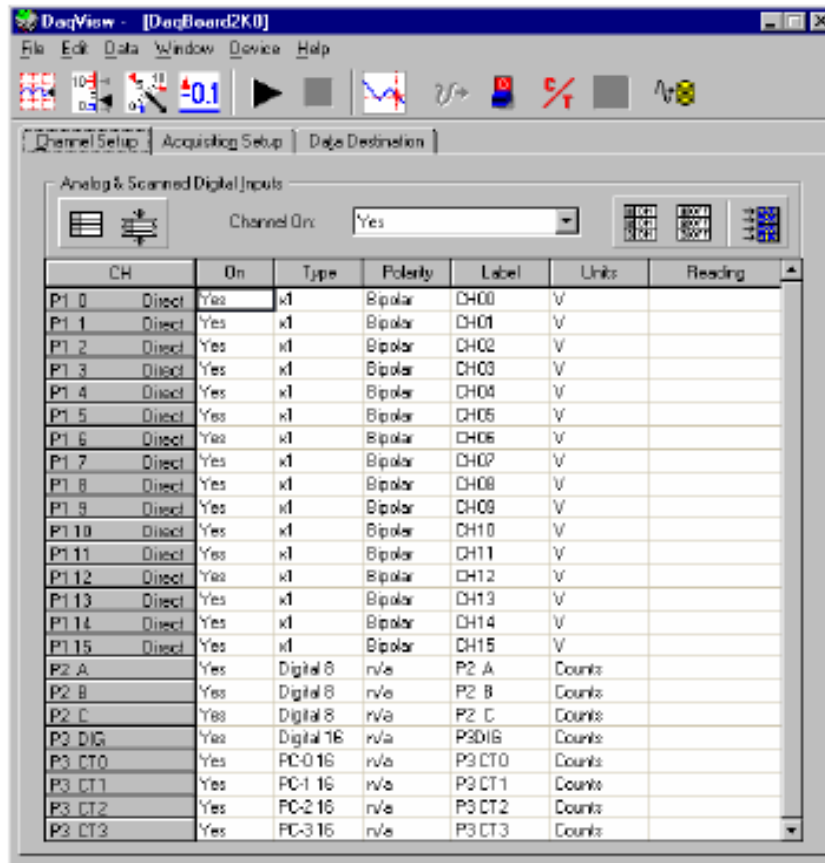


Figure 3.15. Screen shot of Daqview data acquisition software.

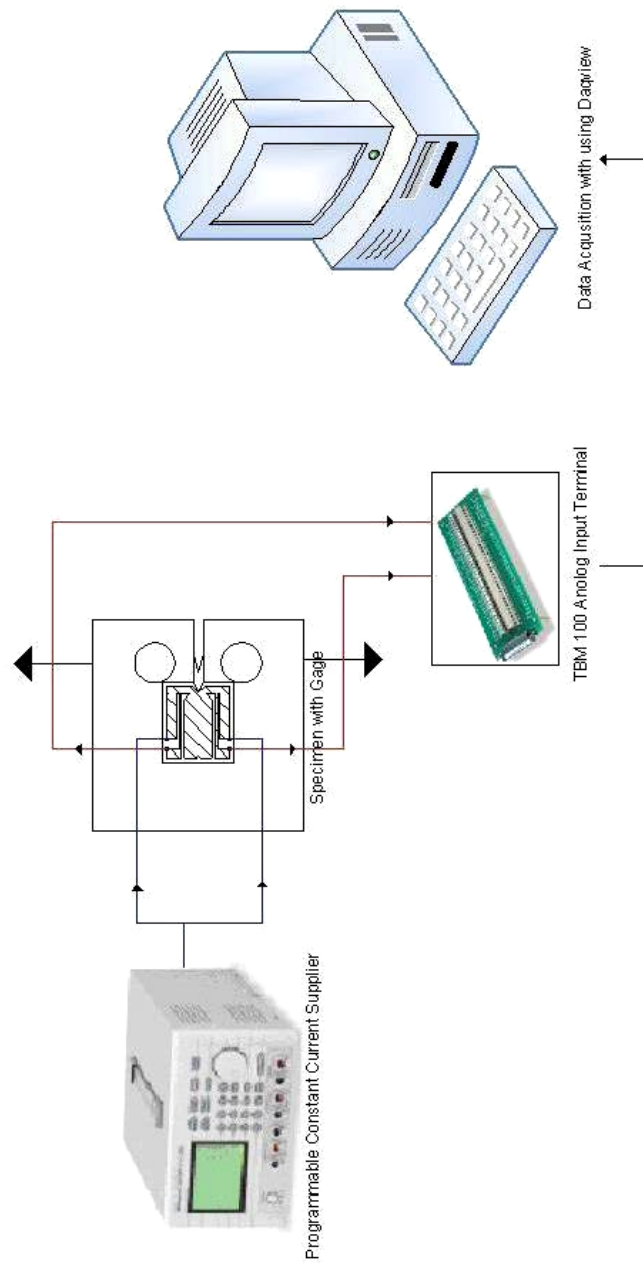


Figure 3.16. Scheme of test set-up.

CHAPTER 4

RESULTS AND DISCUSSION

4.1. Natural Aging and Overaging Heat Treatments

Apart from the as received T651 condition, the bulk material was solutionized at 538 °C for 90 minutes in an air convection furnace and water quenched in order to investigate the fatigue crack growth behavior of the AA6013 according to the different heat treatment conditions. The water quenched plate was naturally aged at room temperature for 96 hours to reach T42 condition. After T42 was confirmed by hardness and conductivity tests, the plate was divided in to two parts, and one of the parts is kept in T42 condition while the other was aged at 245 °C for 12 hours to achieve an overaged condition (TOA). Hardness and conductivity measurements were done after heat treatments. A hardness profile was obtained from the overaging treatment, see Figure 4.1. In addition, the conductivity change during the TOA heat treatment is shown in 4.2 respectively.

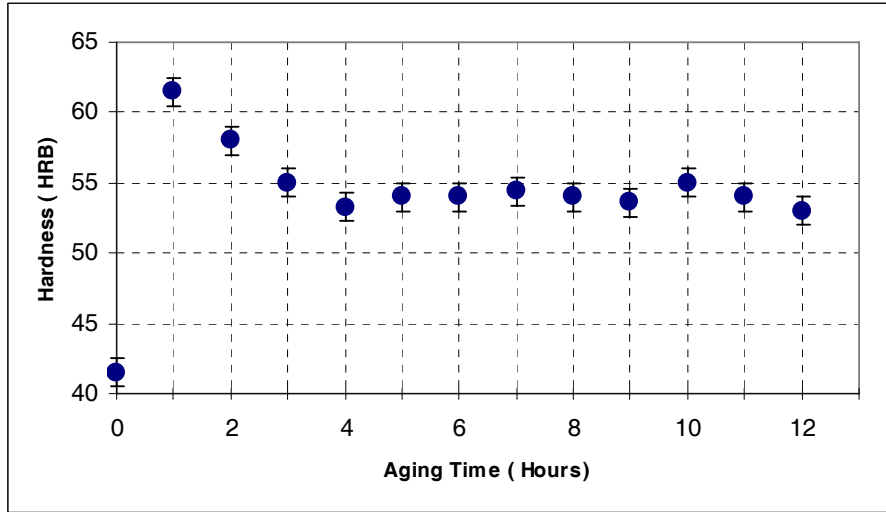


Figure 4.1. Hardness Profile of AA6013 T42 alloy during aging at 245 °C.

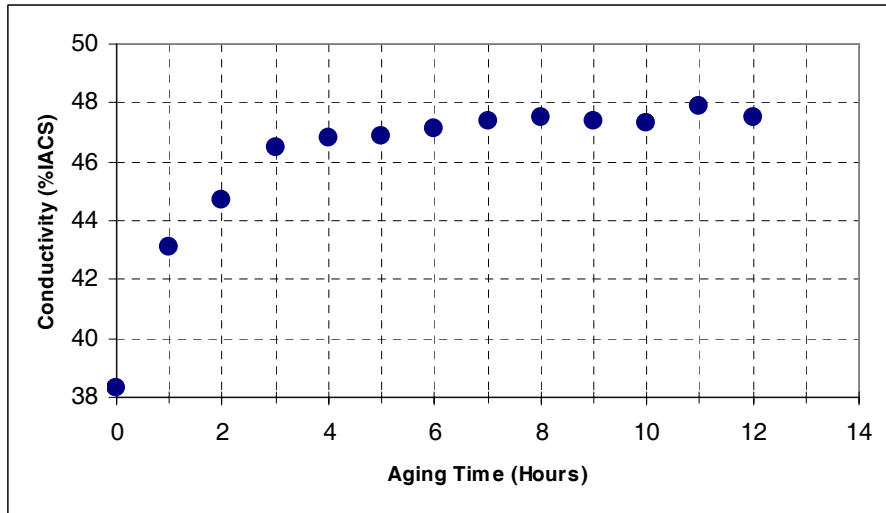


Figure 4.2. Conductivity change of AA6013 T42 alloy during aging at 245 °C.

It can be clearly seen that hardness of the material increased significantly in the first hour of the treatment. It is estimated that during the first hour material was aged to the peak condition, which is normally aging at 191 °C for 4-5 hours according to SAE AMS 2770G [24]. After first hour hardness was decreased, this may be attributed to the increase in precipitate size.

An electrical conductivity measurement of an aluminum alloy determines its conductivity in ohm centimeters or in percent of the International Annealed Copper Standard (IACS) by comparison with certified conductivity standards. For a properly identified aluminum alloy, electrical conductivity measurement is a nondestructive method for verifying heat treatment. The electrical conductivity test used in conjunction with hardness testing makes it feasible to verify proper heat treatment [33]. Two different hardness conditions can provide the same conductivity reading in % IACS.

Conductivity of the alloy increased with aging time (Figure 4.2.). Conductivity is a property that many parameters can affect. Not only the precipitates sizes and distribution is important but also the grain size influence the conductivity of a metal. So that a material can reach same conductivity at different hardness values.

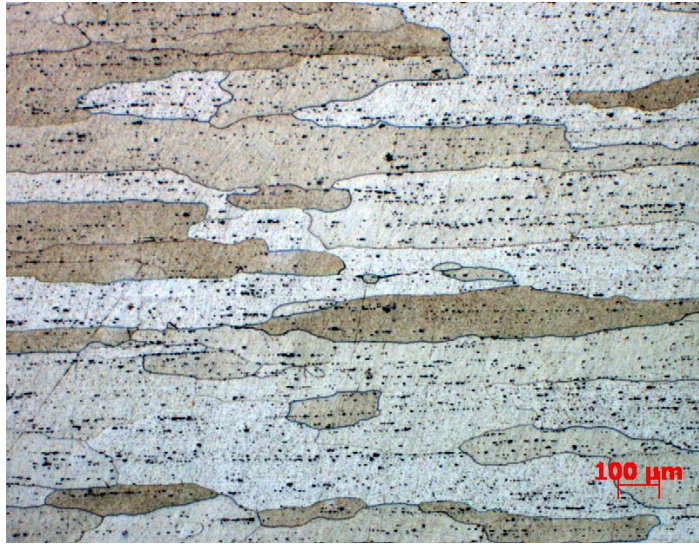
The complete comparison table for hardness and conductivity values is given in Table 4.1.

Table 4.1. Hardness and conductivity values for three different heat treatment conditions.

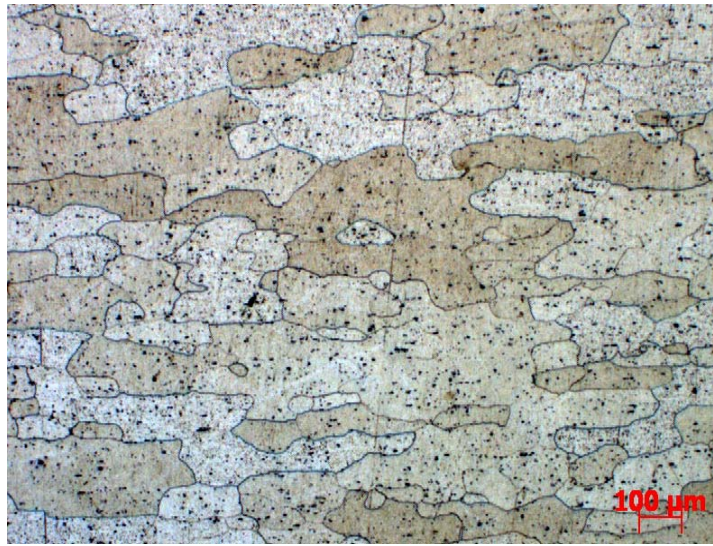
	AA6013 T651	AA6013 T42	AA6013 TOA
Hardness, HRB	70-72	40-42	52-54
Conductivity, % IACS	42.5	38.3	47.5

4.2. Metallographic Examination

The micrographs of different heat treatment conditions, T651, T42, TOA, in longitudinal, L and transverse, T directions are shown in Figure 4.3, 4.4, 4.5, respectively.



(a)

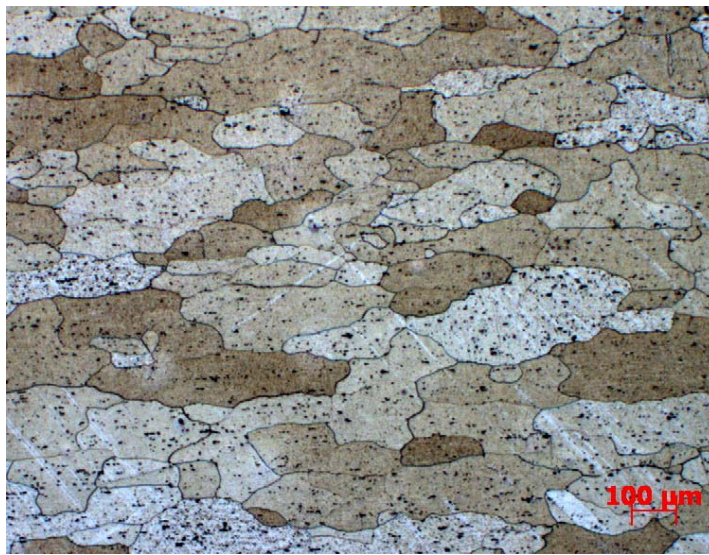


(b)

Figure 4.3. Micrograph of T651 condition a) in longitudinal b) in transverse.

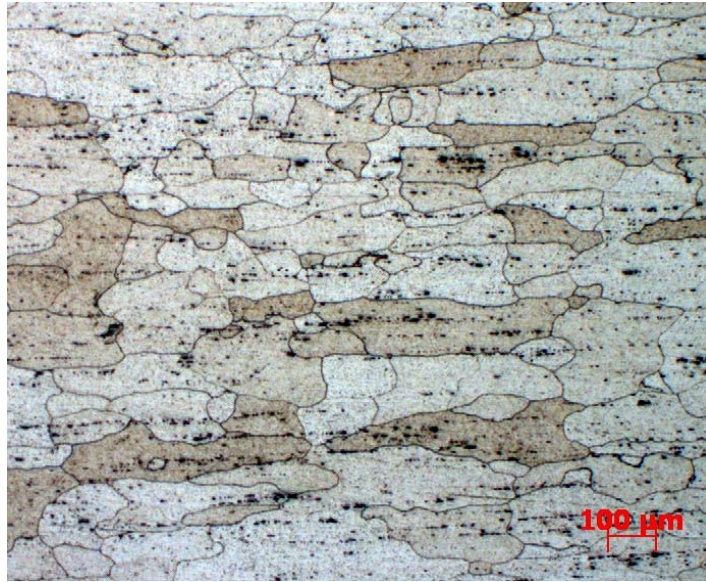


(a)



(b)

Figure 4.4. Micrograph of T42 condition a) in longitudinal b) in transverse.



(a)



(b)

Figure 4.5. Micrograph of TOA condition a) in longitudinal b) in transverse.

It is clear that all heat treated specimens have elongated grains in their microstructure due to the rolling operation. Because of solution heat treatment all elongated, longer grains grew and got partly equaxed after the heat treatment of other two conditions T42 and TOA. Moreover, the elongated particles which were lined up during rolling had never been dissolved and reoriented during solutinizing so that all three conditions have fine particles lined up in rolling direction those are believed to be Mg_2Si and Fe_3SiAl_2 particles. In the longitudinal, L direction equaxed grains observed, where the intermetallic particles of Mg_2Si are lined in the rolling direction, which proves the orientation. The equaxed grains on the surface in L direction can be explained by the recrystallization during rolling. Nevertheless, in the depth of the plate elongated grains can be clearly observed.

4.3. Mechanical Properties

Tension tests were applied, according to ASTM E 8M-04 [26], to characterize the mechanical properties of the material after the heat treatment and to compare those with its original peak aged condition; results are shown in Table 4.2.

Table 4.2. Tensile properties of AA6013 in different for different heat treatment conditions and orientations.

		UTS (MPa)	σ_y (MPa)	Elon. (%)
T651	T	397 ± 3	355 ± 4	5 ± 1
	L	395 ± 5	350 ± 4	6 ± 1
T42	T	303 ± 3	154 ± 6	42 ± 2
	L	302 ± 1	152 ± 6	39 ± 1
TOA	T	303 ± 1	252 ± 9	12 ± 1
	L	297 ± 1	251 ± 1	13 ± 1

Although there is no significant change between orientations of same conditions, there are significant changes in yield strengths and elongations between different heat treatment conditions. Highest tensile and yield strengths are observed in the peak aged condition T651 as expected. Natural aged condition is the most ductile one with lowest yield strength. Tensile strengths of naturally aged T42 and overaged TOA are close, but yield strength of the overaged TOA condition is higher than that of the natural aged one.

The K_{Ic} values of the three heat treatment conditions according to their orientations were calculated with the equations, Eq. 4.1 and 4.2 in ASTM B 399-90 [27]. Measured K_{Ic} values are shown in Table 4.3.

$$K_Q = \left(\frac{P_Q}{BW^{1/2}} \right) f(a/W) \quad (4.1)$$

$$f(a/W) = \frac{(2 + a/W)(0.886 + 4.64a/W - 13.32a^2/W^2 + 14.72a^3/W^3 - 5.6a^4/W^4)}{(1 - a/W)^{3/2}} \quad (4.2)$$

Table 4.3. Plain strain fracture toughness values of AA6013 under different conditions.

Condition \ Orientation	T651	T42	TOA
T-L	38.0 MPa m ^{1/2}	38.5 MPa m ^{1/2}	46.8 MPa m ^{1/2}
L-T	39.0 MPa m ^{1/2}	40.4 MPa m ^{1/2}	59.4 MPa m ^{1/2}

The fracture toughness tests were achieved in T-L and L-T orientations for naturally aged and overaged conditions. Values are higher in L-T orientation and overaged condition has the highest toughness value. Peak aged K_{Ic} values were reported in ASM Alloy Digest [34].

4.4. Determination of Stress Intensity Range

For the stress intensity range calculations ASTM E 647-00 [29] standard suggests a formula given below.

$$\Delta K = \frac{\Delta P}{BW^{1/2}} \frac{(2+a/W)}{(1-a/W)^{3/2}} (0.886 + 4.64a/W - 13.32a^2/W^2 + 14.72a^3/W^3 - 5.6a^4/W^4) \quad (4.3)$$

This expression is valid for $a/W \geq 0.2$ where the crack length a , is the average value of the two surfaces measured by gage.

Maximum stress intensity, K_{max} , values for all specimens were also calculated. To calculate K_{max} critical crack lengths were measured after the tests. Critical crack length is the length of the crack just before the fracture takes place, which was out of the crack gage limit in this study, so that crack lengths were measured by calipers. Table 4.4 shows K_{max} values for all conditions.

Table 4.4. Maximum stress intensity range, K_{max}

Heat Treatment	K_{max} , (MPa.m ^{1/2})	
	T-L	L-T
T651	63.6	69.3
T42	51.1	56.6
TOA	51.4	62.4

Maximum stress intensity values are higher than the values obtained from tests, because the test values are calculated within the gage limits but K_{max} values were calculated with the crack lengths measured outside gage limits.

4.5. Crack Length vs. Number of Cycle Curves

Crack length measurements were done by crack gages on the both sides of the specimens during the experiments. With the average of the collected data, crack length versus number of cycles graphics were plotted. Curves for peak aged, natural aged and overaged condition in T-L and L-T orientations are shown in Figure 4.6-4.8. In Figure 4.9 and 4.10 curves of different heat treatment conditions in same orientations are shown.

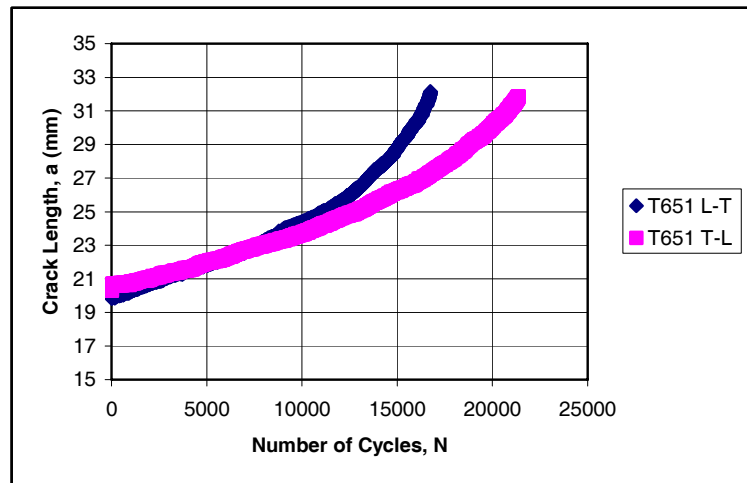


Figure 4.6. Crack length vs. number of cycle curves for T651 L-T and T651 T-L.

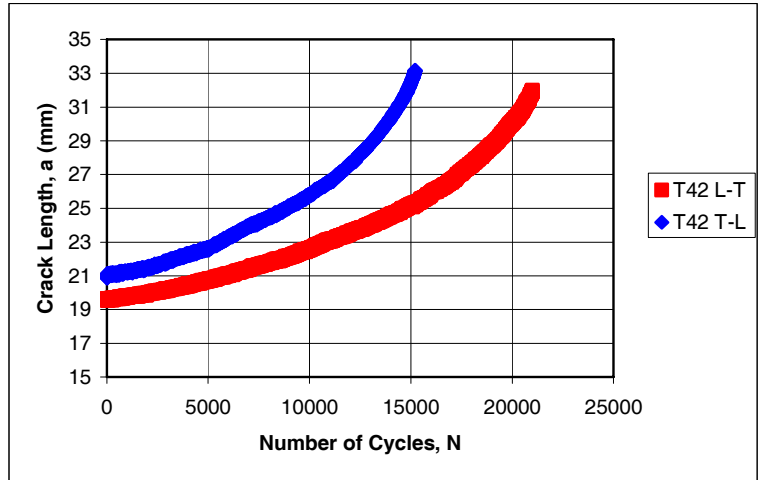


Figure 4.7. Crack length vs. number of cycle curves for T42 L-T and T42 T-L.

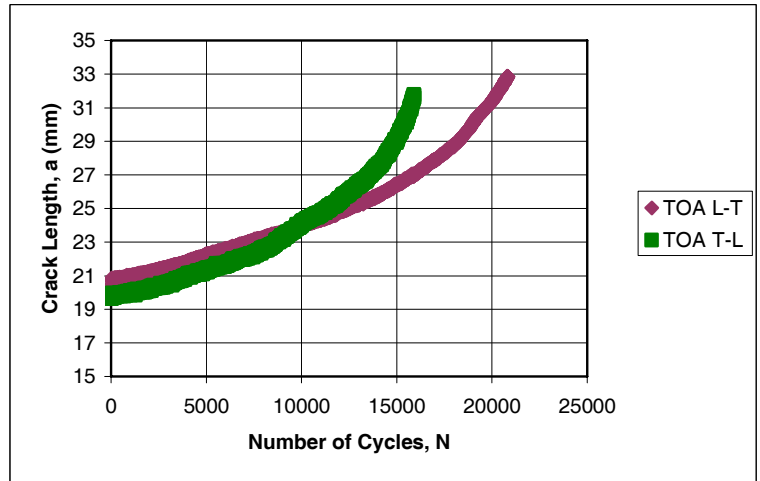


Figure 4.8. Crack length vs. number of cycle curves for TOA L-T and TOA T-L.

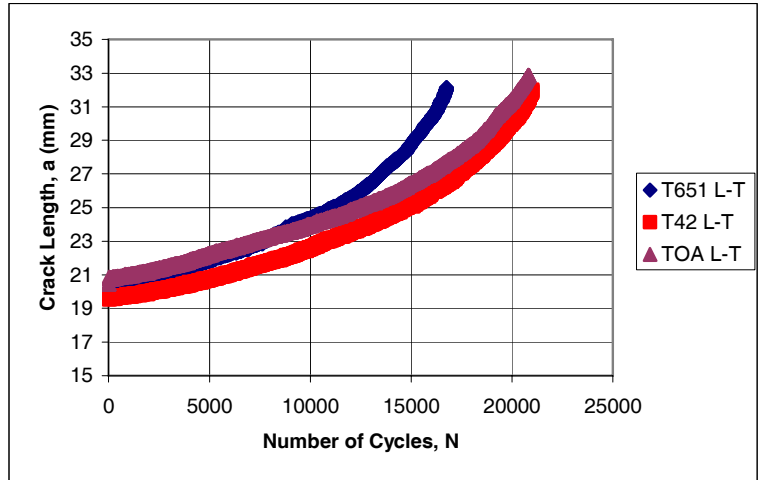


Figure 4.9. Crack length vs. number of cycle curves for all conditions in L-T direction.

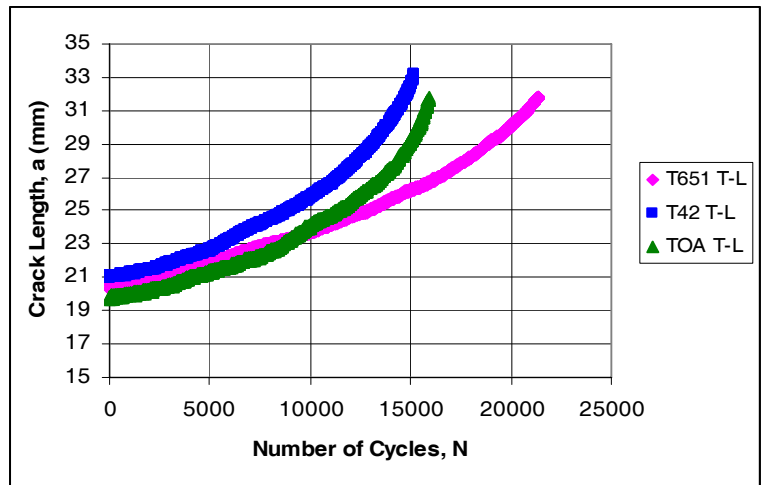


Figure 4.10. Crack length vs. number of cycle curves for all conditions in T-L direction.

4.6. Crack Growth Rate vs. Stress Intensity Range Plots

To plot the crack growth rates vs. stress intensity range curves, first stress intensity ranges and crack growth rates were calculated. Seven-point incremental polynomial technique was used for data reduction. A BASIC computer program whose code is published in ASTM E 647-00 [29] was used for the computation. With the computed data, logarithmic plots of crack growth rate vs. stress intensity range were graphed, Figures 4.11 to 4.16.

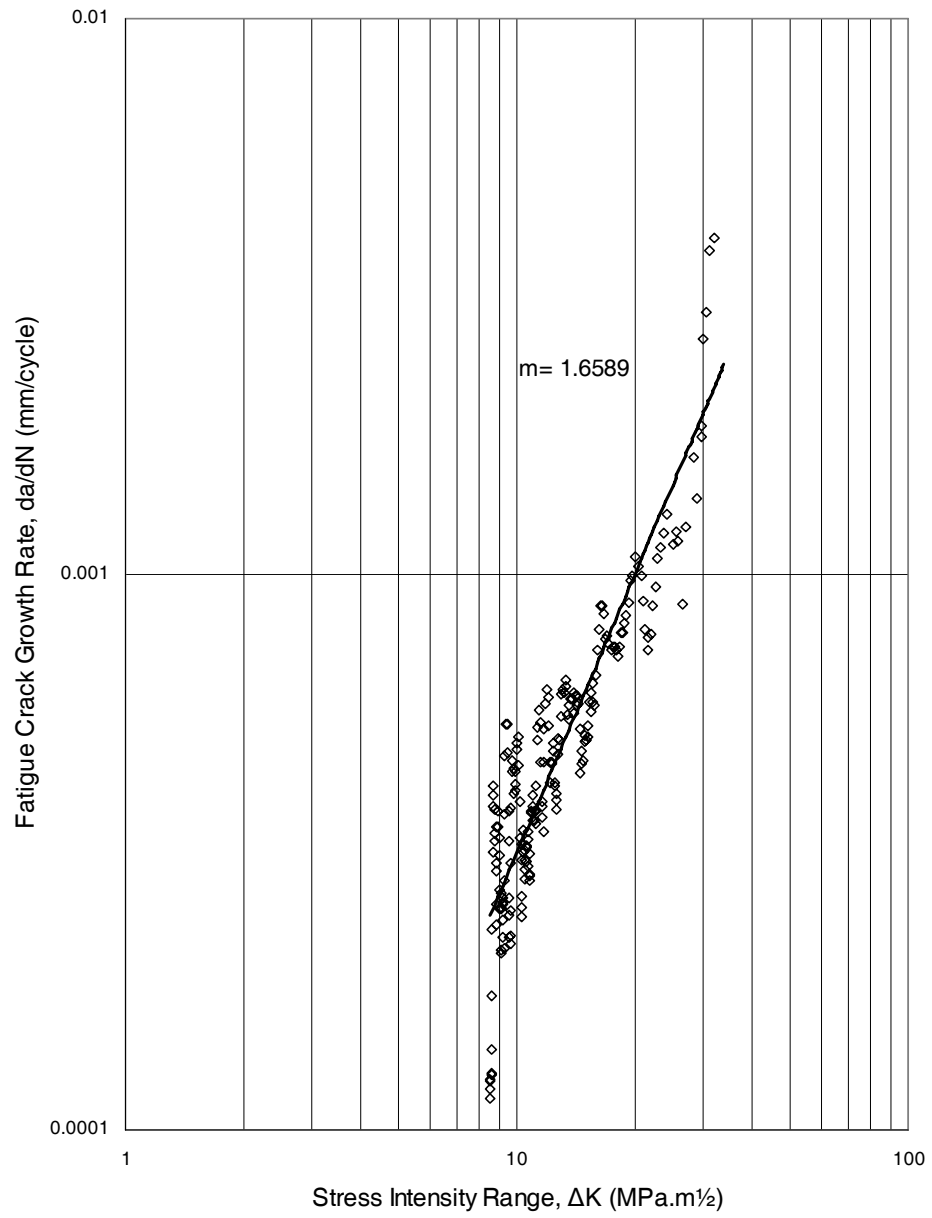


Figure 4.11. da/dN vs. ΔK plot of T651 T-L.

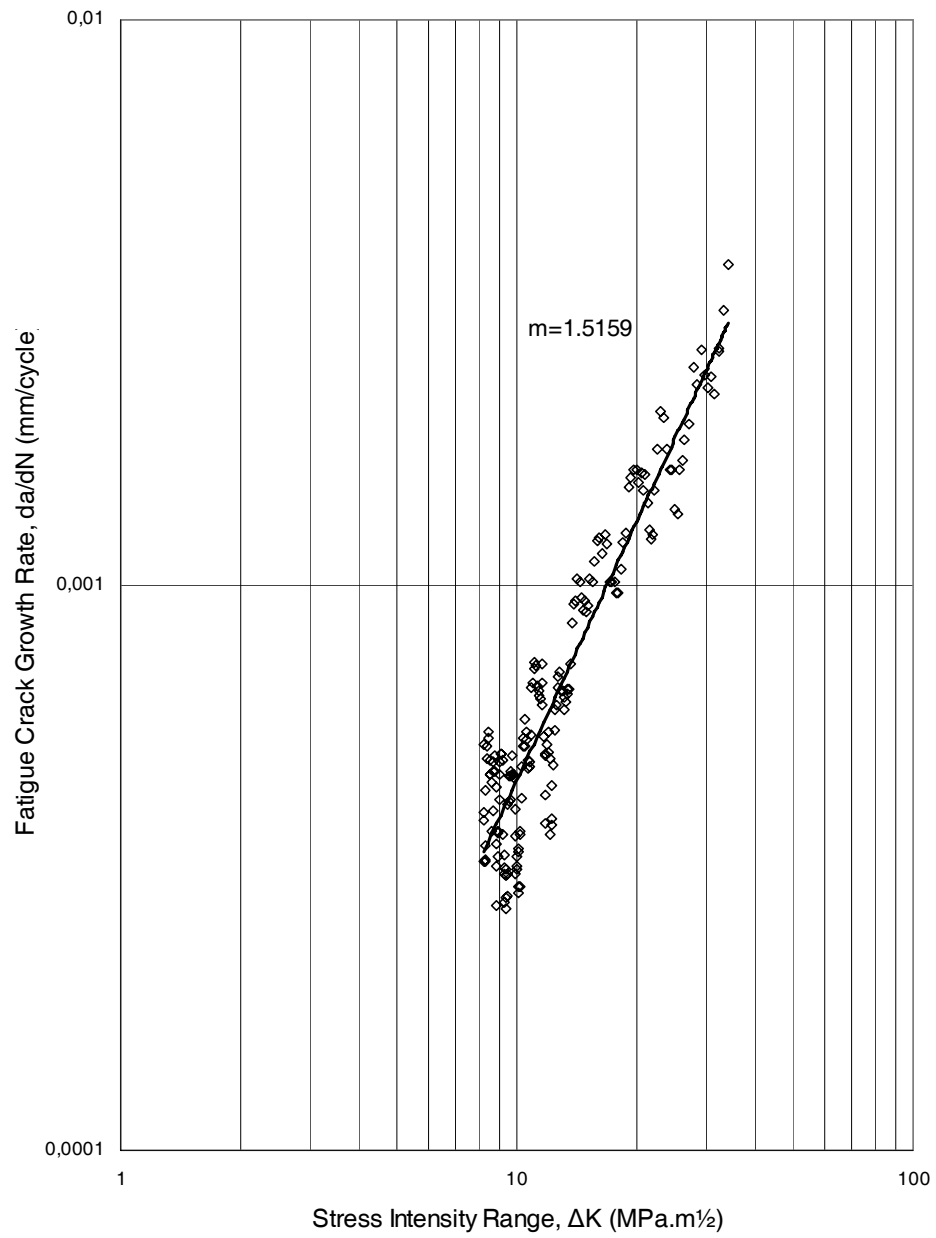


Figure 4.12. da/dN vs. ΔK plot of T651 L-T.

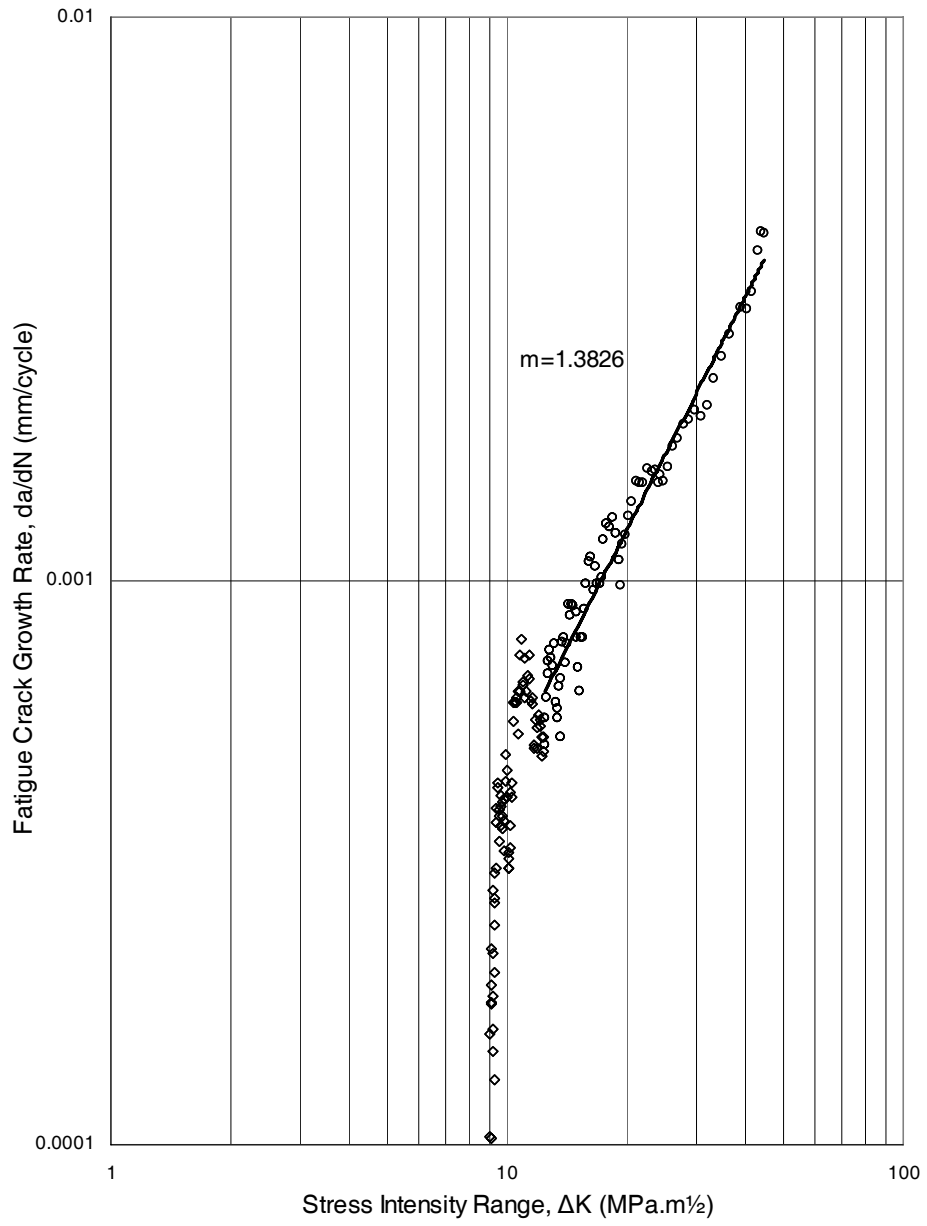


Figure 4.13. da/dN vs. ΔK plot of T42 T-L.

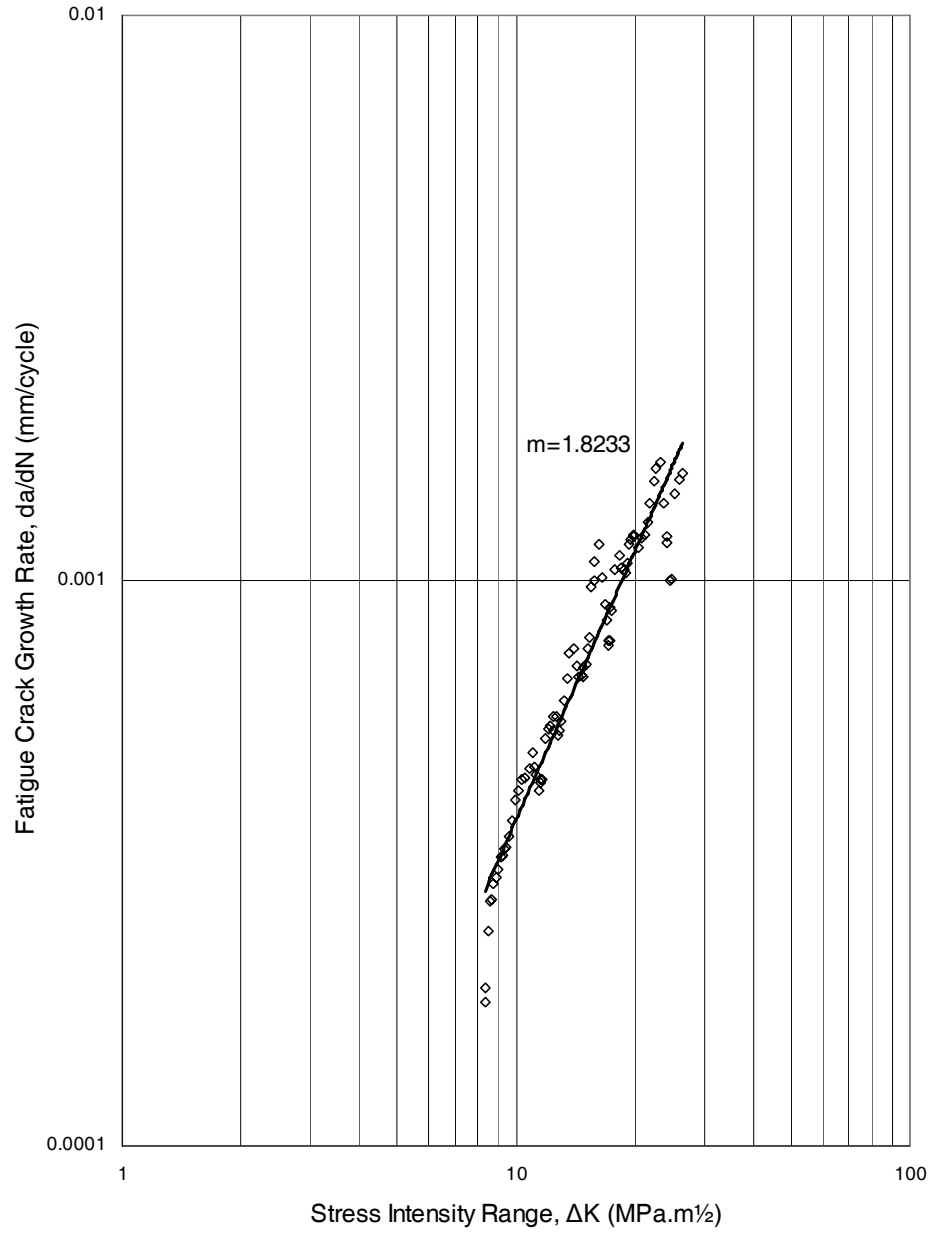


Figure 4.14. da/dN vs. ΔK plot of T42 L-T

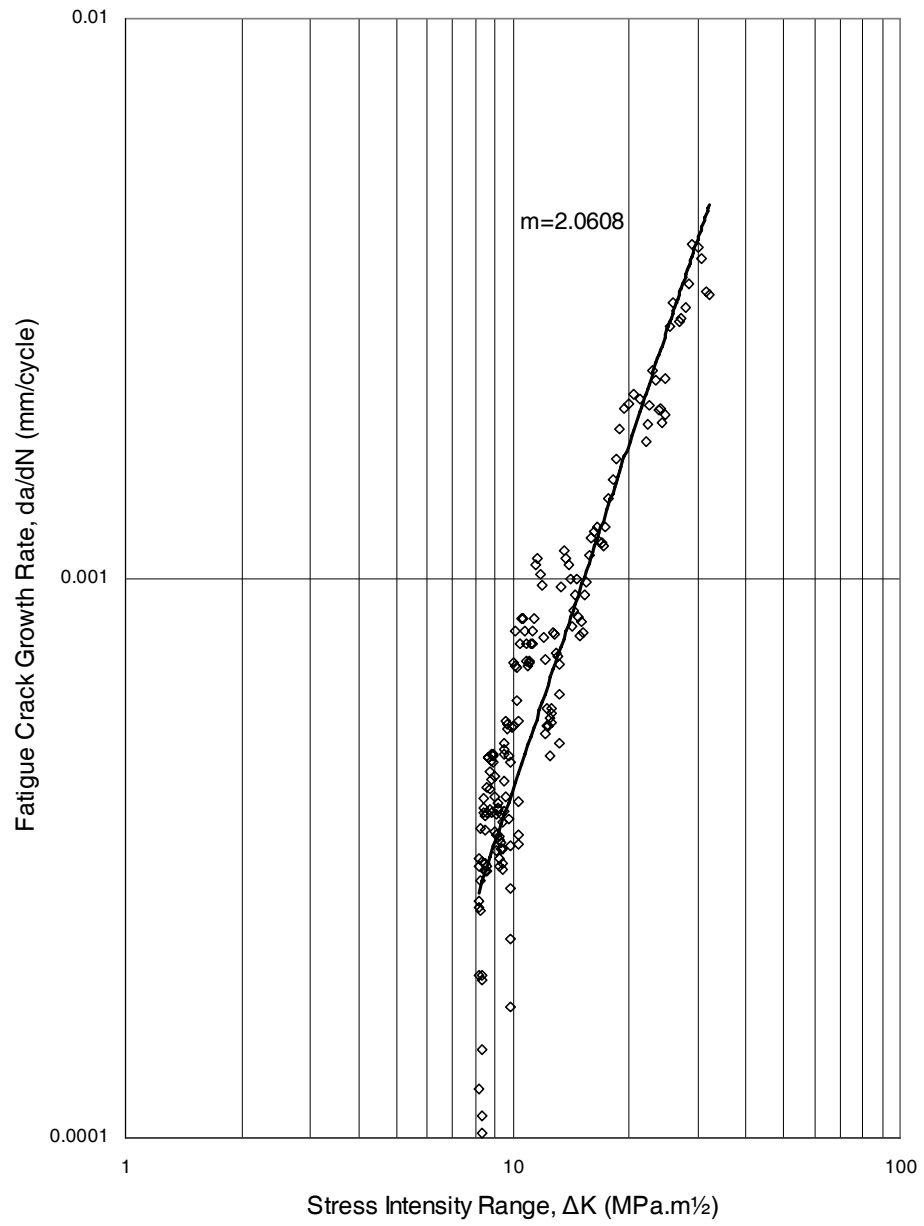


Figure 4.15. da/dN vs. ΔK plot of TOA T-L.

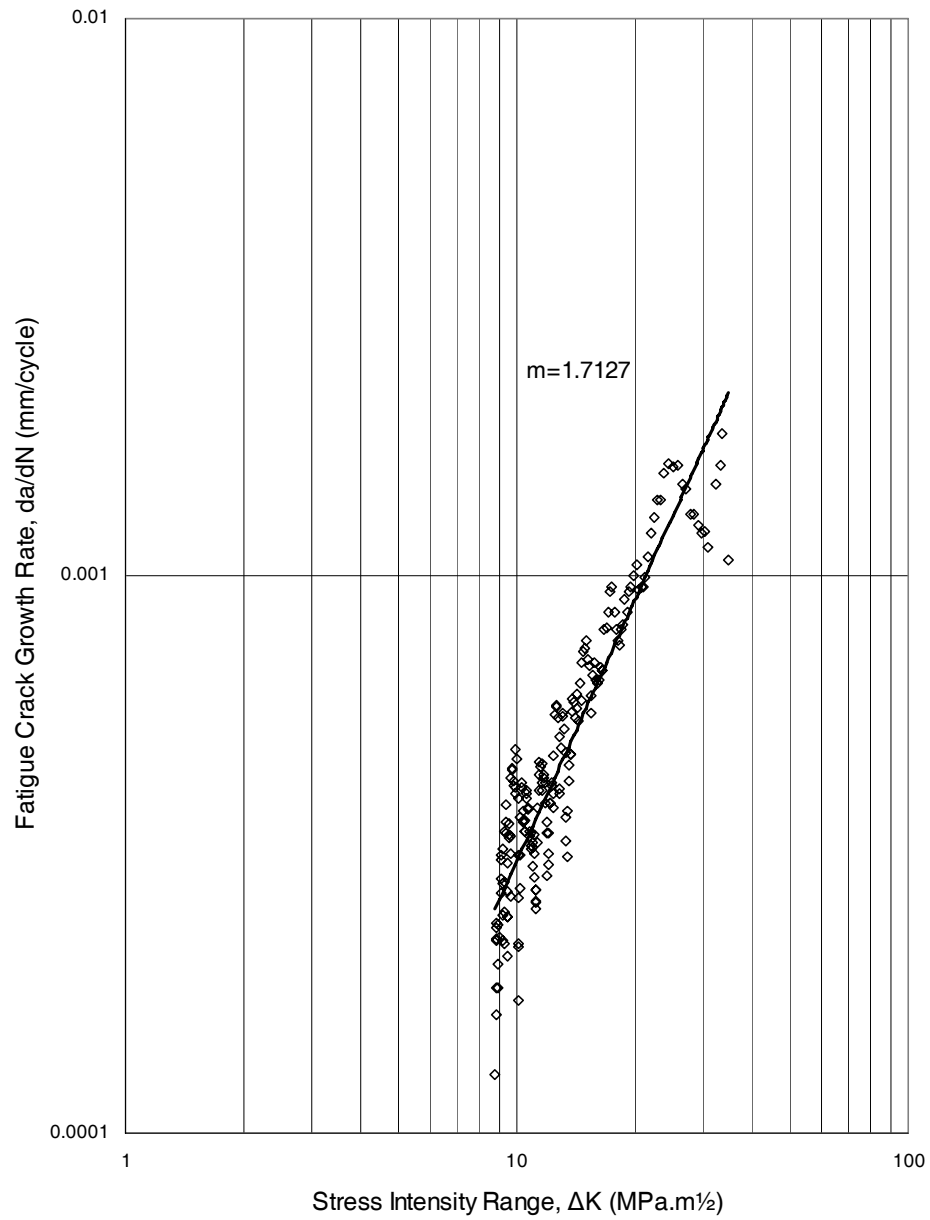


Figure 4.16. da/dN vs. ΔK plot of TOA L-T.

According to the values obtained from plots it is estimated that all conditions have a threshold value of about $K_{th} \approx 8-9 \text{ MPa m}^{1/2}$.

4.7. Application of Paris-Erdogan Law

Paris-Erdogan law was applied to stage II regions of the da/dN vs. ΔK plots to determine the C and m constants in the Paris-Erdogan equation.

$$\frac{da}{dN} = C(\Delta K)^m \quad (4.4)$$

Fitting curves on the stage II regions with linear regression, C and m values were calculated with the Eqn. 4.4 of the fitted power equation. C and m values are tabulated in Table 4.5.

Table 4.5. Paris-Erdogan constants.

Heat Treatment	Orientation	C	m	R ²
T651	T-L	7×10^{-6}	1.6589	0.79
	L-T	1×10^{-5}	1.5159	0.88
T42	T-L	2×10^{-5}	1.3826	0.95
	L-T	5×10^{-6}	1.8233	0.95
TOA	T-L	4×10^{-6}	2.0608	0.87
	L-T	6×10^{-6}	1.7127	0.91

Although the regression values are quite low for some conditions, the computed da/dN values and experimental results are very close, which means stage II regions of the plots obey the Paris-Erdogan law.

4.8. Comparison of the da/dN vs. ΔK Plots

The plots were grouped, in same orientations and in same heat treatment conditions, to compare the effects individually, see Figures from 4.17 to 4.21.

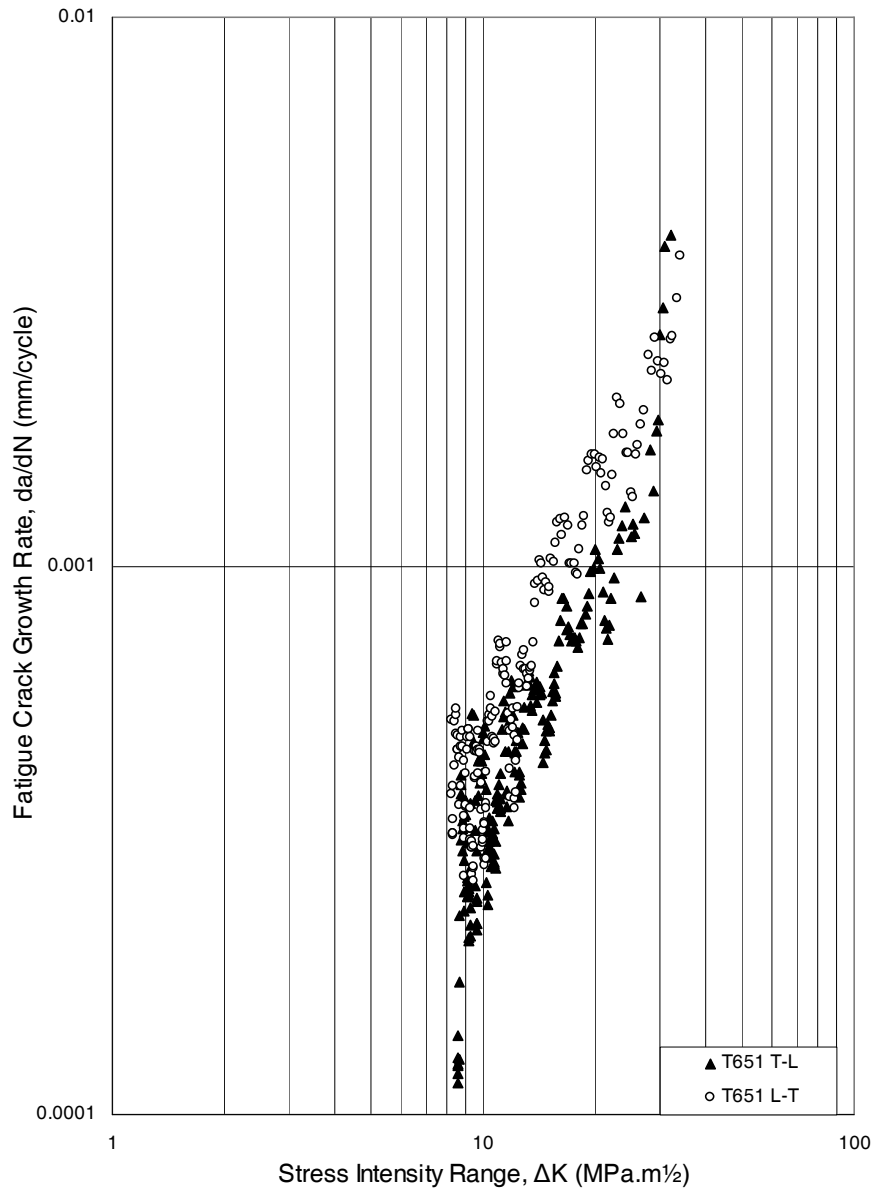


Figure 4.17. da/dN vs. ΔK plot of T651 condition in two orientations.

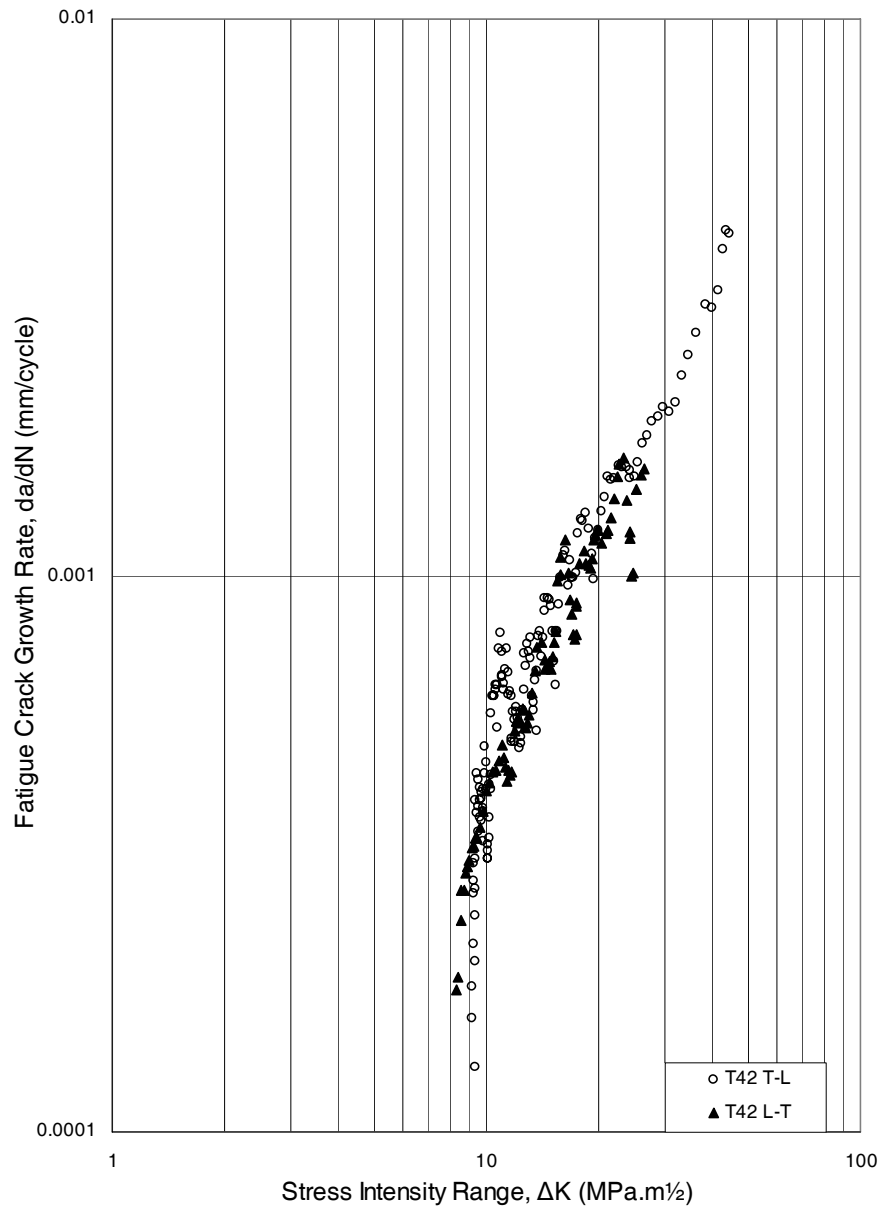


Figure 4.18. da/dN vs. ΔK plot of T42 condition in two orientations.

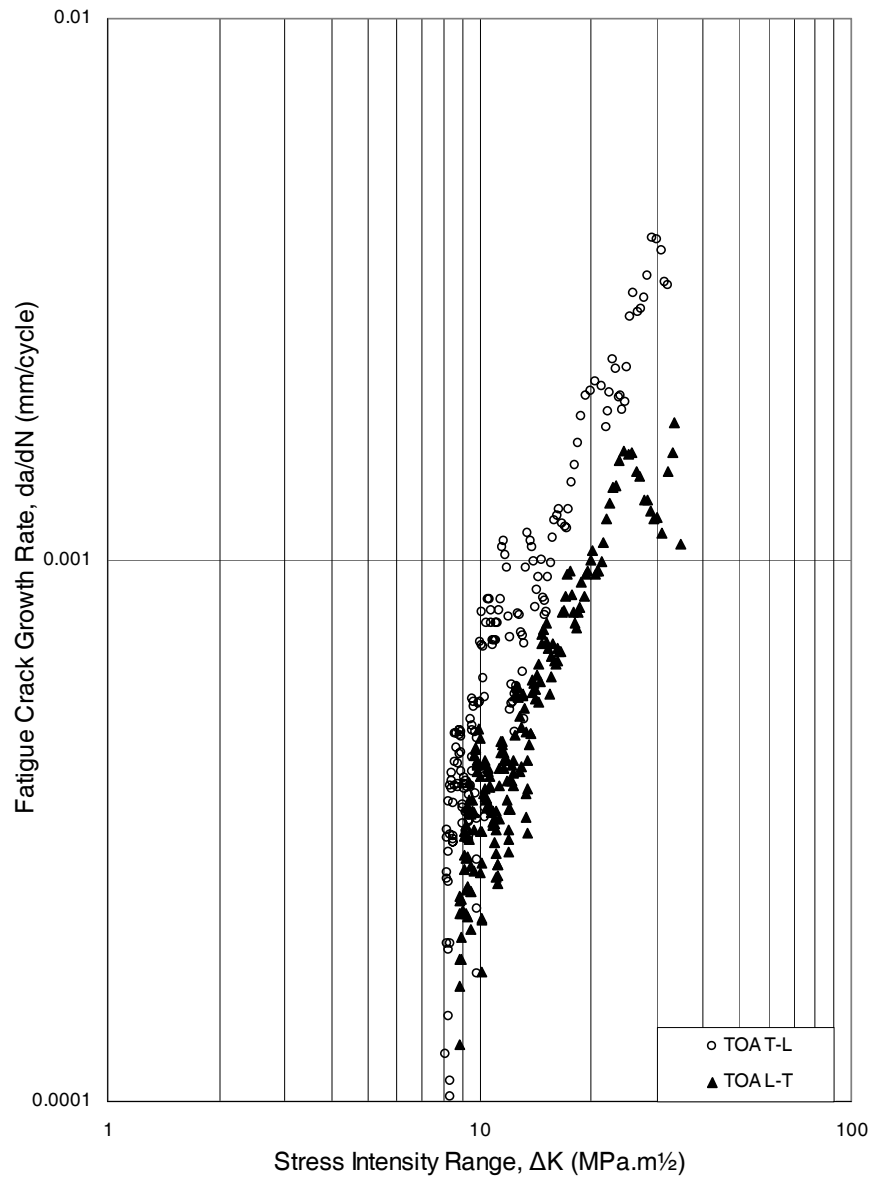


Figure 4.19. da/dN vs. ΔK plot of overaged condition in two orientations.

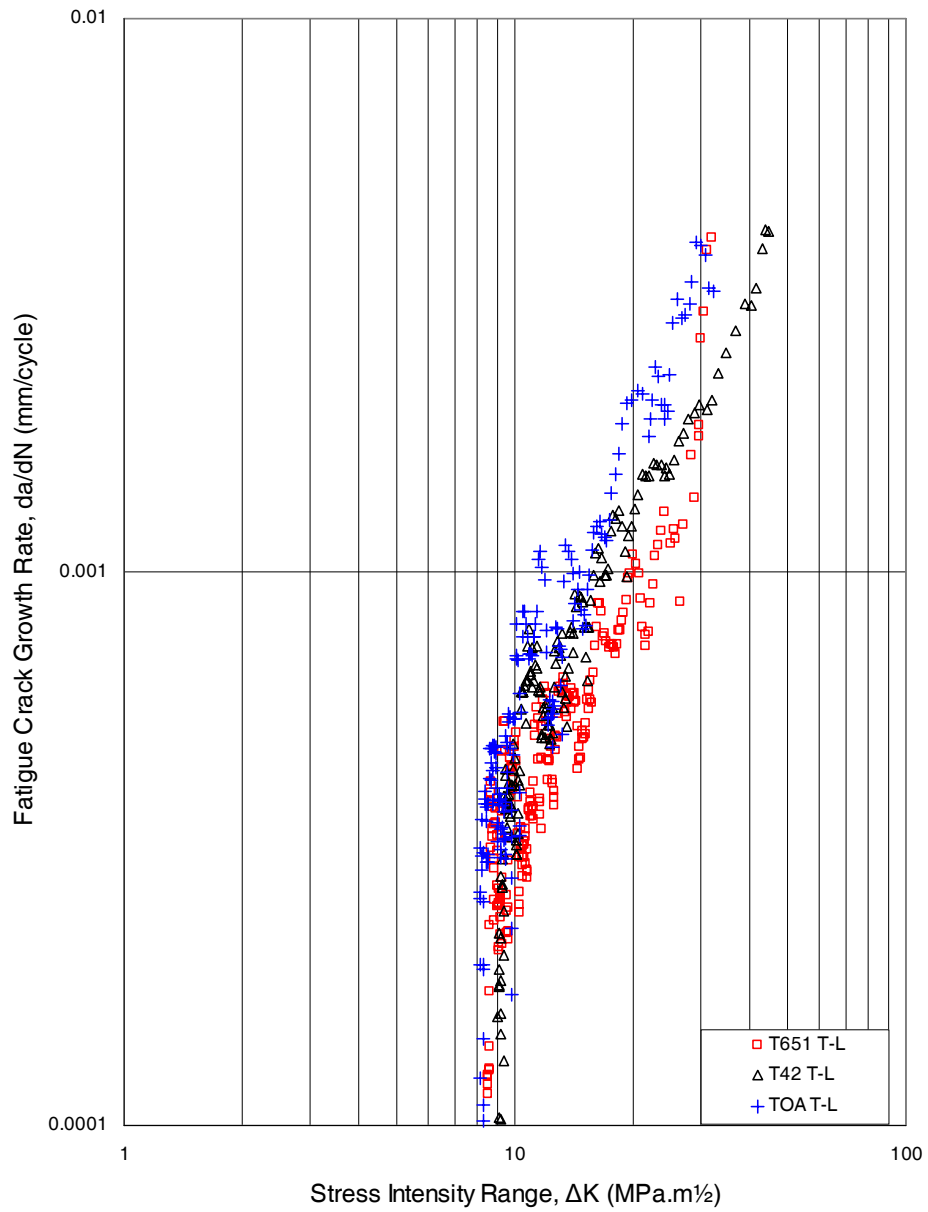


Figure 4.20. da/dN vs. ΔK plots of T651, T42 and TOA condition in T-L orientation.

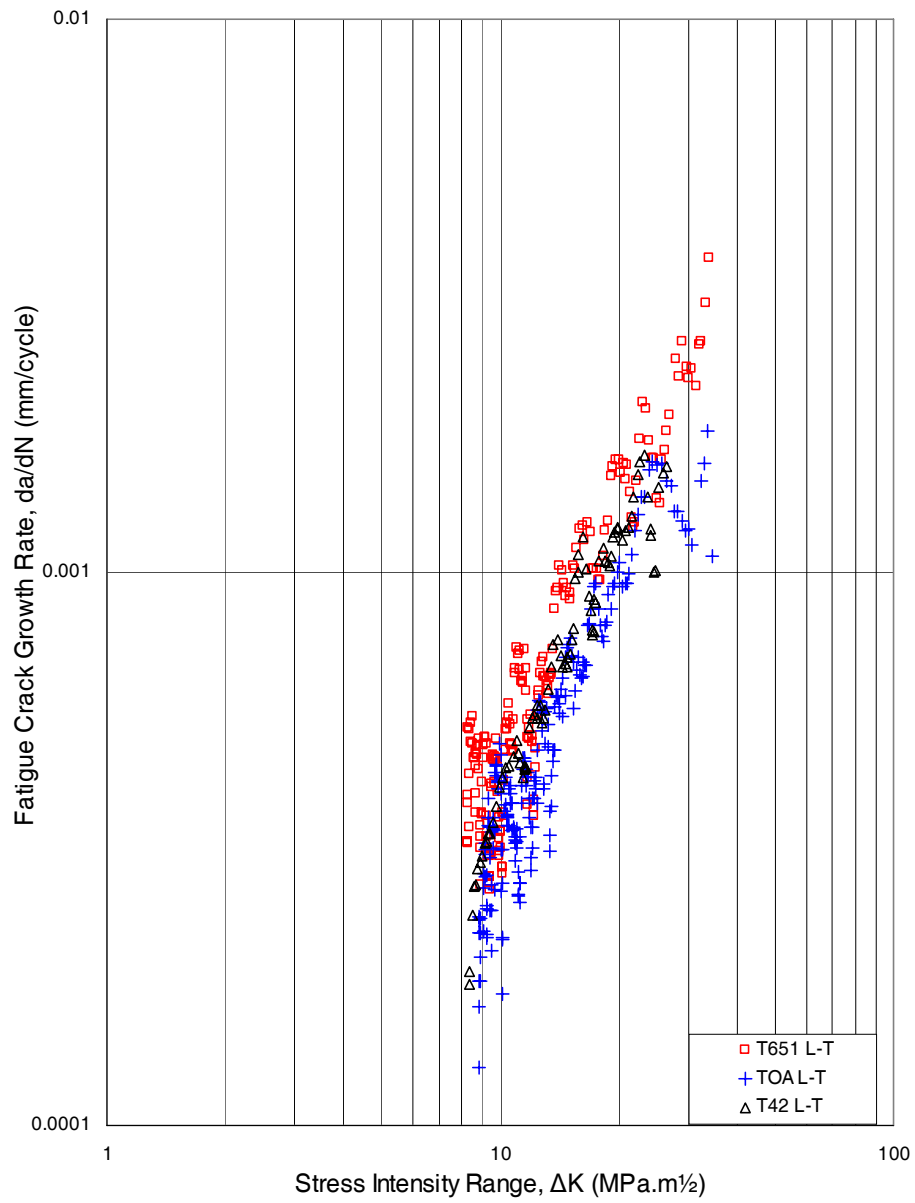


Figure 4.21. da/dN vs. ΔK plots of T651, T42 and TOA condition in L-T orientation.

Comparing the effect of orientation, it is clear that L-T direction specimen in TOA condition has higher resistance to fatigue crack growth rate than the T-L oriented TOA specimen has. In addition, a slight increase in resistance to fatigue crack growth rate is observed in L-T direction of T42 condition. On the contrary, for the T651 condition, fatigue crack growth resistance is worse in the L-T orientation than in T-L orientation.

The orientation dependence of fatigue crack growth rates is significant in all tempers [35]. Crack growth behavior for mode I loading of T-L and L-T cases was studied by other researchers [36]. Their studies showed that crack growth rate was fastest in the T-L specimen occurring throughout the crack growth process. The effect of grain orientation on crack opening for mode I loading was studied as well, indicating that crack tip opening during crack growth for a T-L specimen was 25% lower than for an L-T specimen [36].

It was reported by some authors that the resistance to crack growth is much influenced by the materials microstructure such as the grain orientation and grain boundary. The same studies reported that crack growth rate was different even when the crack was subjected to the same loading parameter of continuum mechanics. The grain boundary acted as the barrier for propagation into adjacent grains [37].

In terms of aging, fatigue crack growth rates of T-L and L-T specimens were compared in Figure 4.20 and 4.21.

For the T-L orientation, T651 condition is the most resistant specimen to fatigue crack growth rate. Fatigue crack growth resistance of the T651 condition significantly advances at the rates faster than 10^{-3} mm/cycle. The fatigue crack growth rate values at the $\Delta K = 20 \text{ MPa}\cdot\text{m}^{1/2}$ of three conditions are shown in Table 4.6. Fatigue crack growth rate of T651 condition in T-L direction is 30% higher

than that of T42 condition and 100% higher than that of TOA condition in the same direction.

Overaged, TOA condition seems to be strongest in terms of fatigue crack growth rate in L-T direction. On the contrary, T651 has fastest in fatigue crack growth rate in L-T direction. TOA condition is 20% slower than T42 and 60% slower than T651 condition for L-T direction.

Table 4.6. Fatigue crack growth rate, da/dN (mm/cycle), values of T651, T42 and TOA conditions at $\Delta K = 20 \text{ MPa.m}^{1/2}$.

Condition \ Orientation	da/dN (mm/cycle)	
	T-L	L-T
T651	0.0010	0.0016
T42	0.0013	0.0012
TOA	0.0020	0.0010

Consequently, the fatigue resistance of the T651 T-L and TOA L-T are higher than the others. Especially in the T42 and TOA conditions, which have equaxed grains, L-T specimens have higher resistance to the crack growth. There is no doubt, that the weakest condition is the TOA in T-L direction.

4.9. Macro Photographs of the Fracture Surfaces

Following the tests, macro photographs of the fracture surfaces were taken. Figures 4.22 to 4.24 show the macro photographs of the surfaces.



Figure 4.22. From left to right, fracture surfaces of the T651 T-L and L-T specimens.

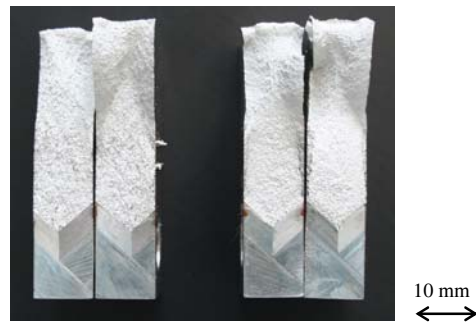


Figure 4.23. From left to right, fracture surfaces of the T42 T-L and L-T specimens.



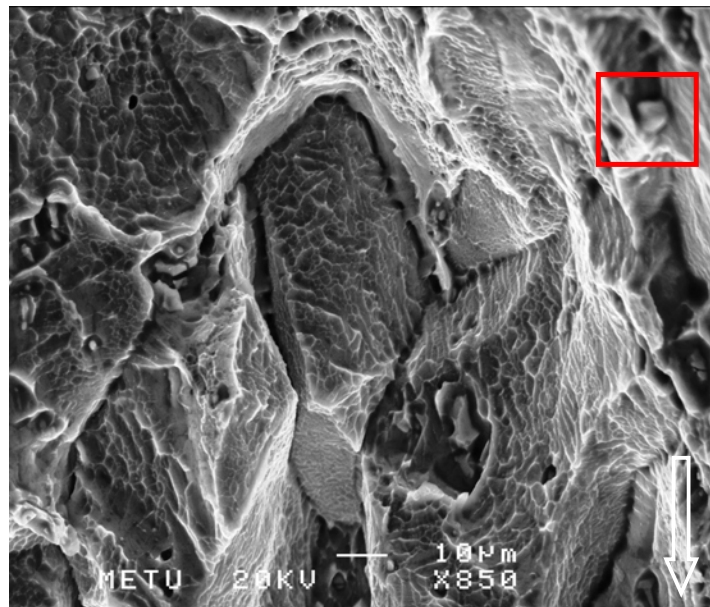
Figure 4.24. From left to right, fracture surfaces of the TOA T-L and L-T specimens.

4.10. Fractographic Analysis

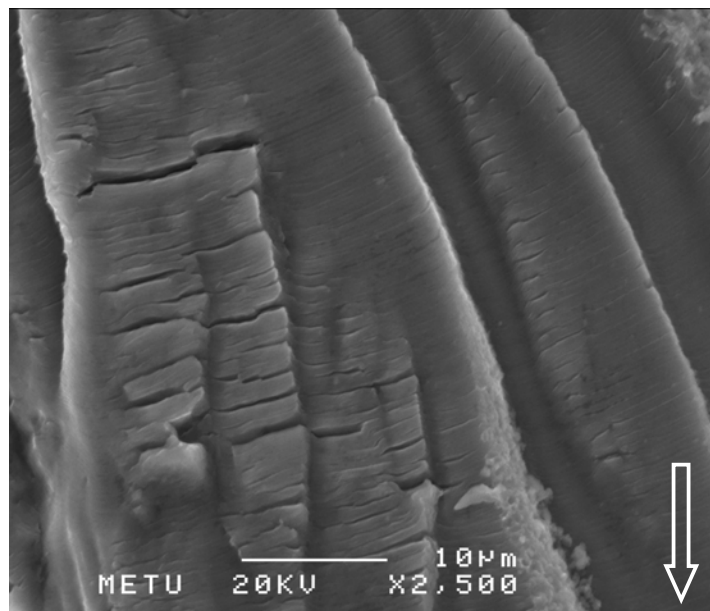
The fracture surfaces of the specimens were examined by the scanning electron microscope (SEM). The micrographs are given in the Figures 4.14 to 4.24. A white down arrow on the photographs shows the crack growth direction. Moreover, in some photographs the directions of the microcrack growth directions are indicated with black arrows.

Fatigue results in very distinctive fracture appearances. In general, there are three different features that can be observed; the initial zone of fatigue, the fatigue crack growth zone and the final fracture due to overload.

In addition to the SEM imaging, energy dispersive spectrum (EDS) analysis was also conducted in this study to analyze the chemical composition and detect some dispersion. The EDS analysis results of such inclusions are given in Figure 4.36 and 4.37.



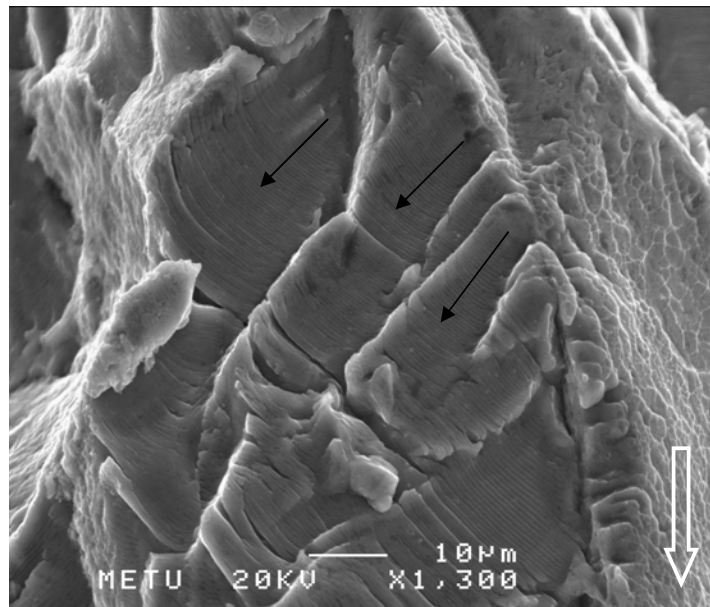
(a)



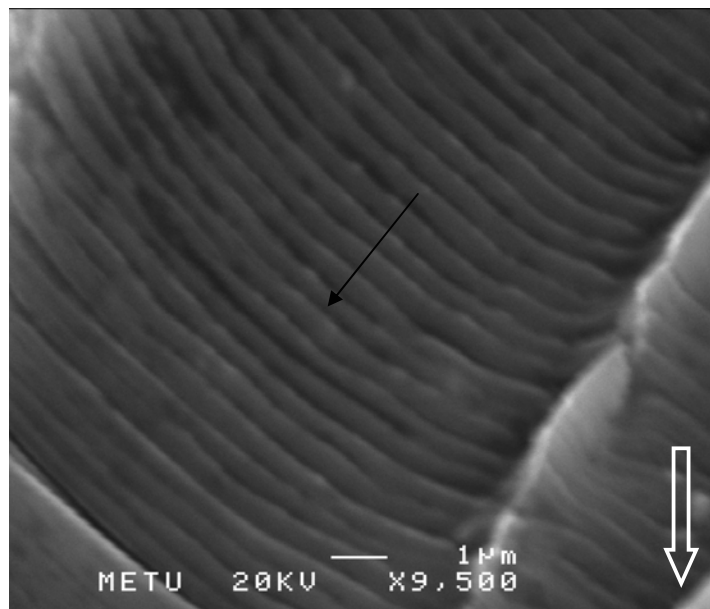
(b)

Figure 4.25. SEM photographs of T651 T-L specimen.

- a) General view of fracture surface with dimples and an intermetallic particle is marked.
- b) Tear ridges on different planes and formation of secondary cracks between striations.



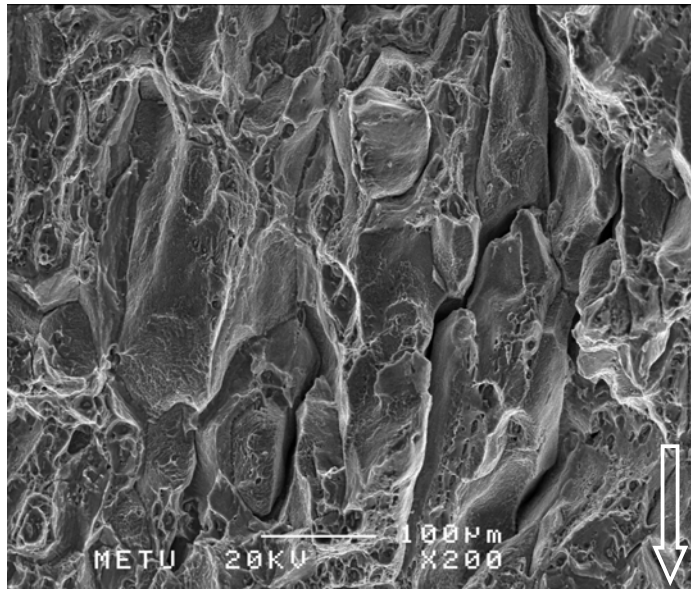
(a)



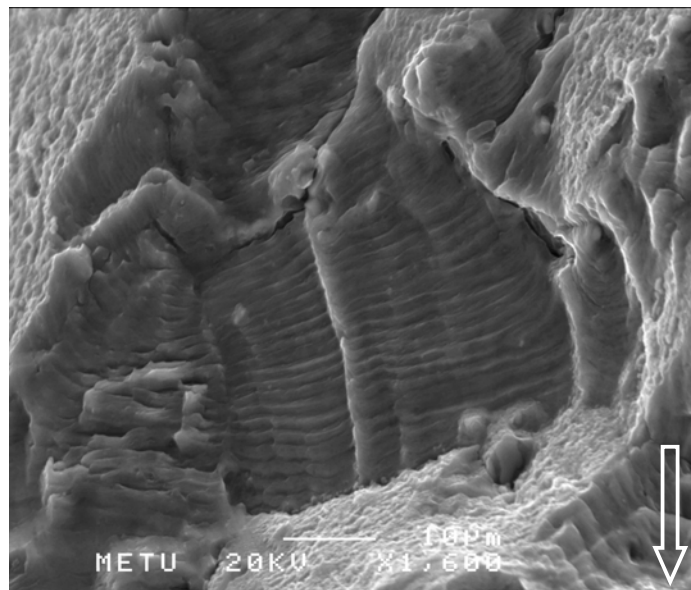
(b)

Figure 4.26. SEM Photographs of T651 T-L specimen.

- a) Dimples, striations, and tear ridges in the same region show a mixed mode fracture, black arrows show local microcracks growth direction.
- b) Close look to the striations at slower regions of stage II, FCGR $\approx 5 \times 10^{-4}$ mm/cycle (measured from photo).



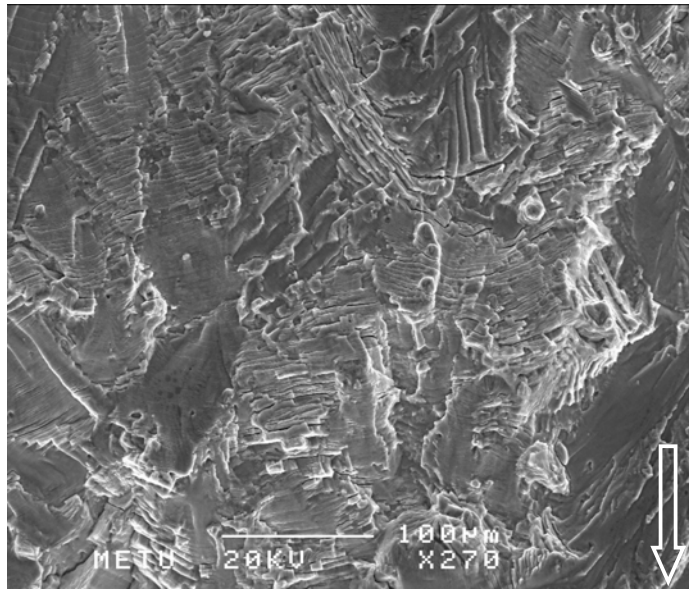
(a)



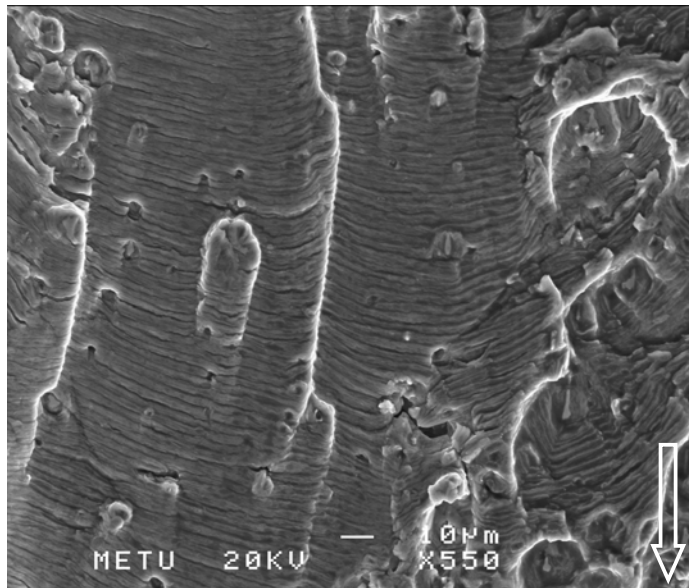
(b)

Figure 4.27. SEM Photographs of T651 T-L specimen.

- a) Micrograph from the fast fracture zone.
- b) The vertical face is apparently a very large tear ridge or cleavage step joining two areas of dimpled rupture, mixed type fracture micrograph from the end of stage II region, FCGR $\approx 1.4 \times 10^{-3}$ mm/cycle (Measured from photo).



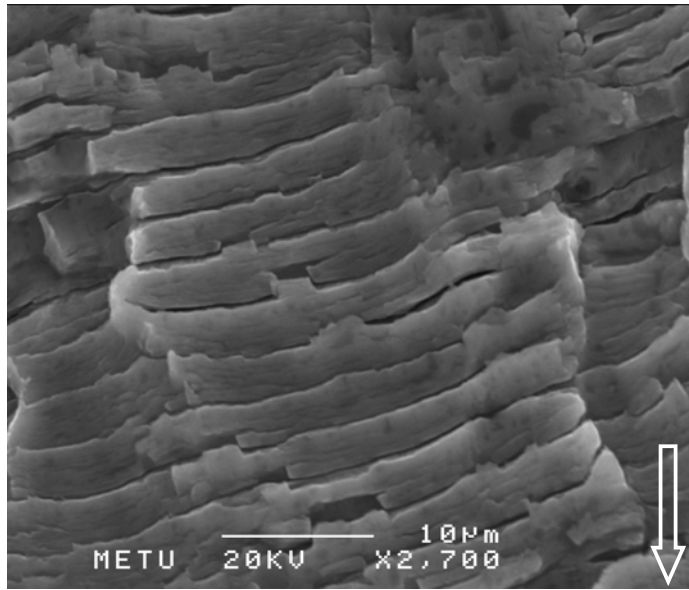
(a)



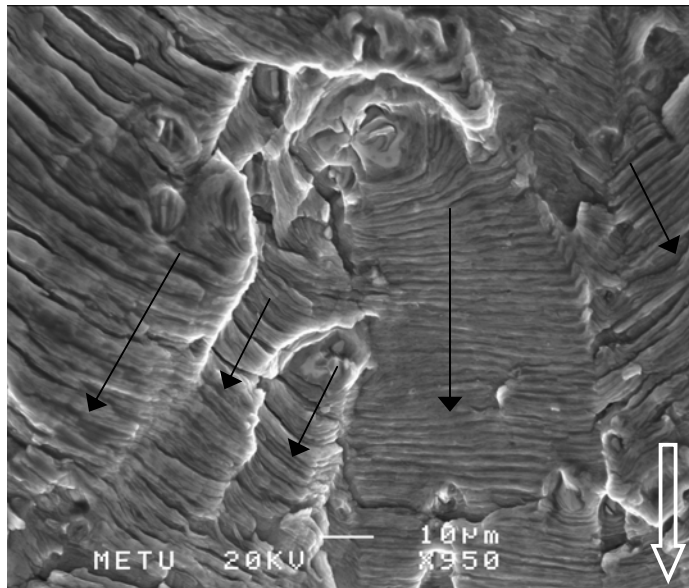
(b)

Figure 4.28. SEM photographs of T42 L-T specimen.

- a) General appearance of fracture surface, growth direction of microcracks in many ways like a turbulent view.
- b) Fatigue striations on the tear ridges in the high da/dN zone, $FCGR \approx 3 \times 10^{-3}$ mm/cycle (measured from photo).



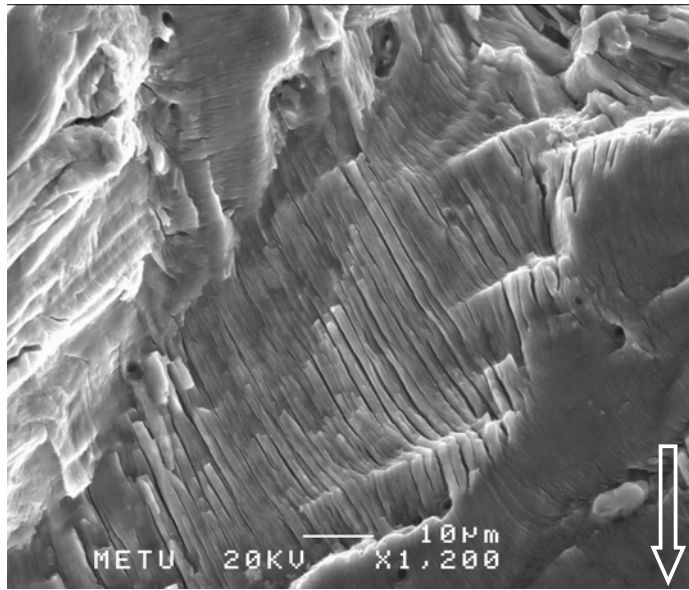
(a)



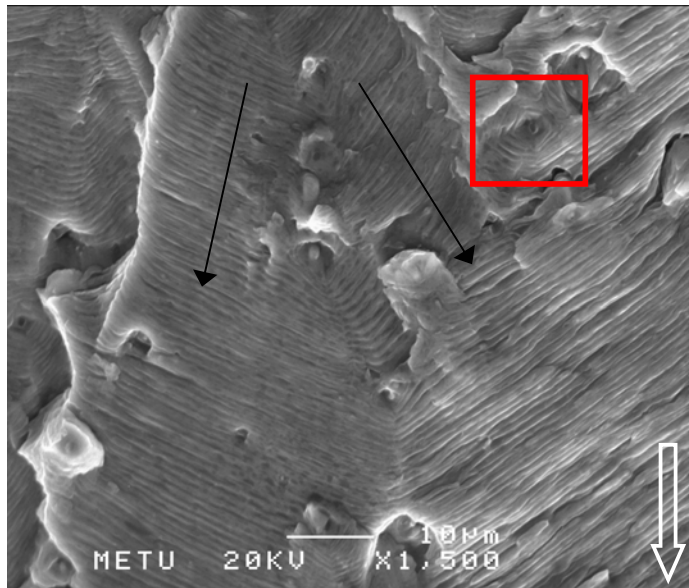
(b)

Figure 4.29. SEM photographs of T42 L-T specimen.

- a) Close up photograph of fatigue striations, local microcracks propagating in different ways.
- b) Secondary crack formations between fatigue striations, microcracks propagating in different ways.



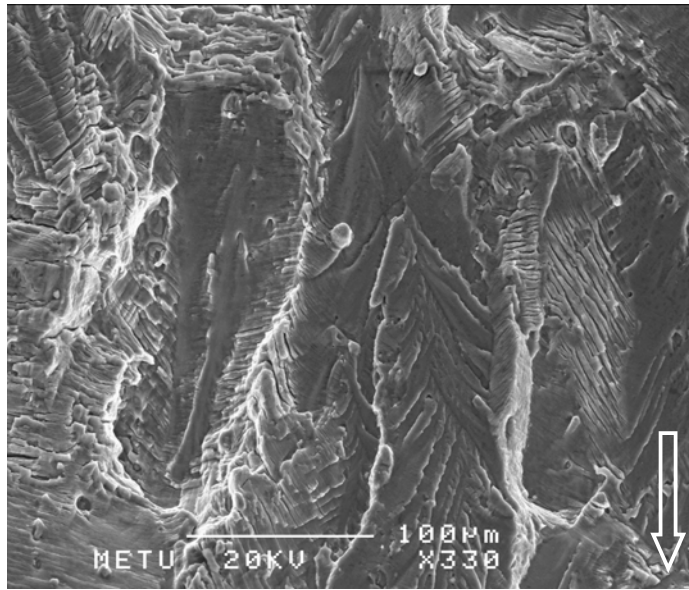
(a)



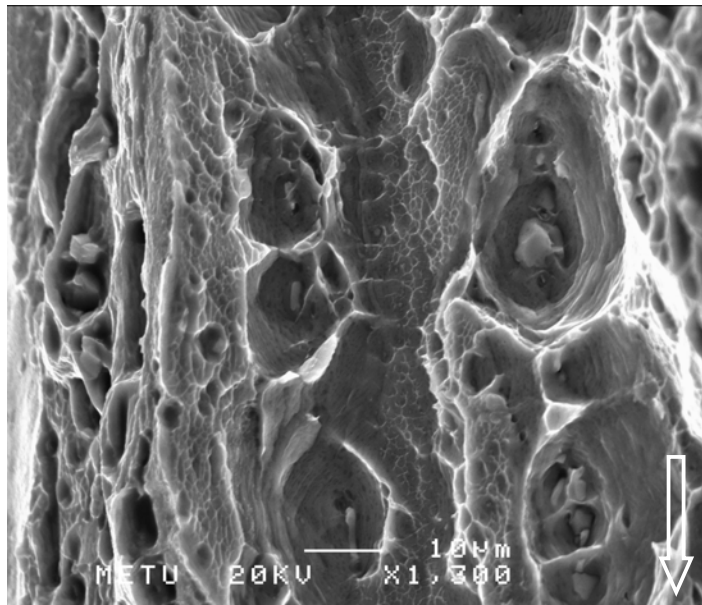
(b)

Figure 4.30. SEM photographs of T42 L-T specimen.

- a) Brittle striations in the fracture zone.
- b) Striations at the Stage II region, black arrows show two different local microcracks is propagating in different ways, an intermetallic particle surrounded by striations, particle marked in a square.



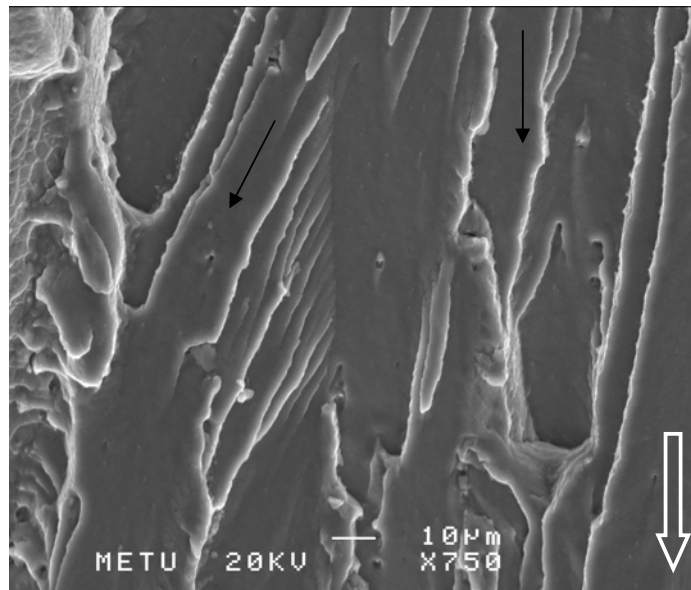
(a)



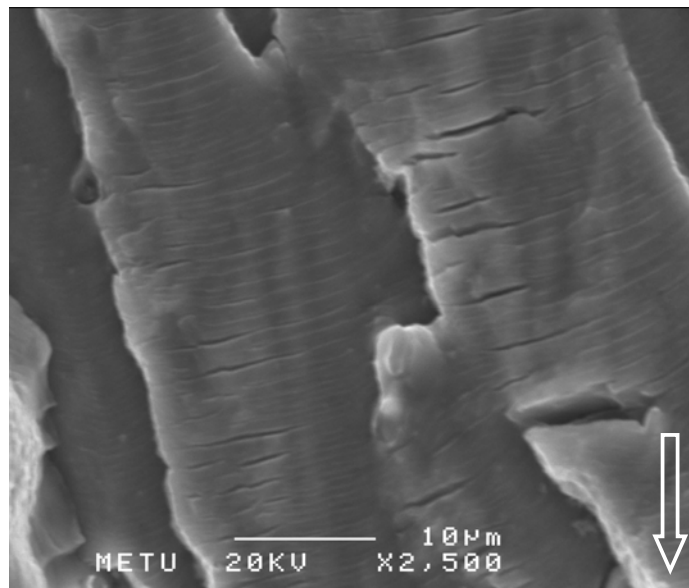
(b)

Figure 4.31. SEM photographs of T42 T-L

- a) General view of the fracture zone, coalescence of different crack growth planes.
- b) Microvoid coalescence, dimpled rupture in the high crack growth rate, high stress intensity region.



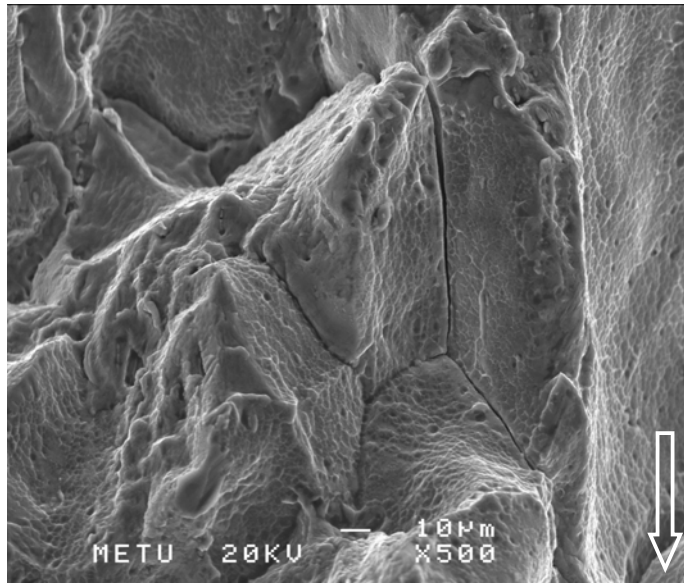
(a)



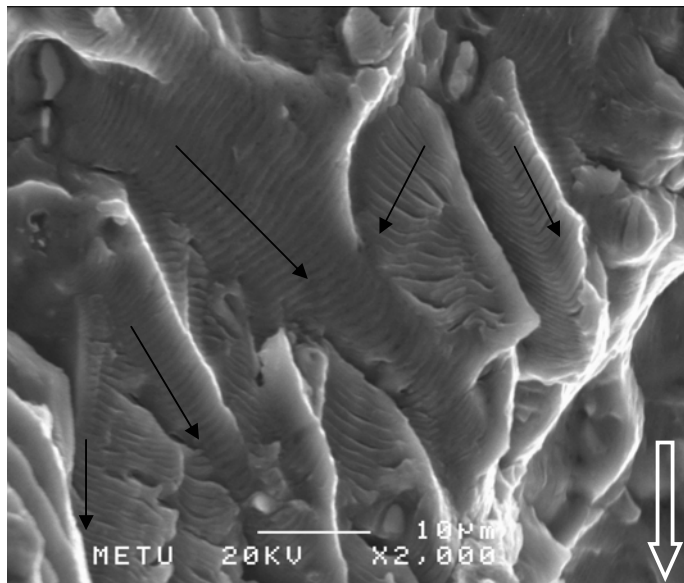
(b)

Figure 4.32. SEM photographs of TOA T-L specimen.

- a) River pattern like fatigue crack growth, coalescence of tear ridges.
- b) Striations in the medium rate region, $FCGR \approx 1 \times 10^{-3}$ mm/cycle (measured from photo).



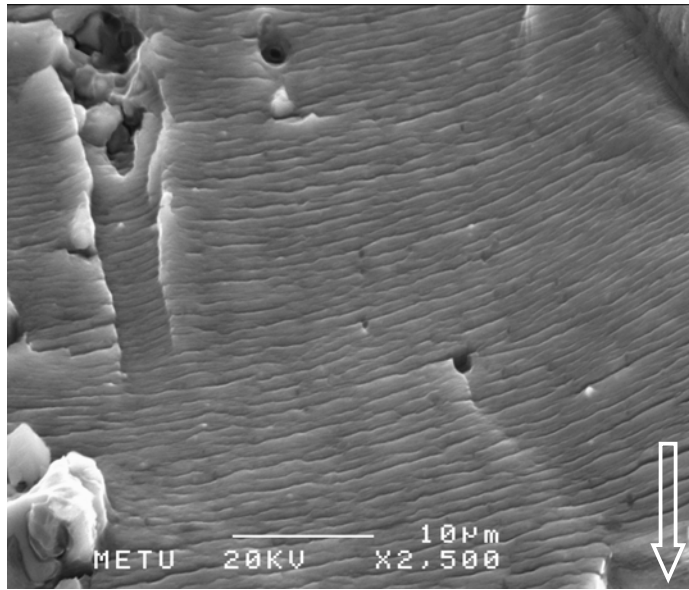
(a)



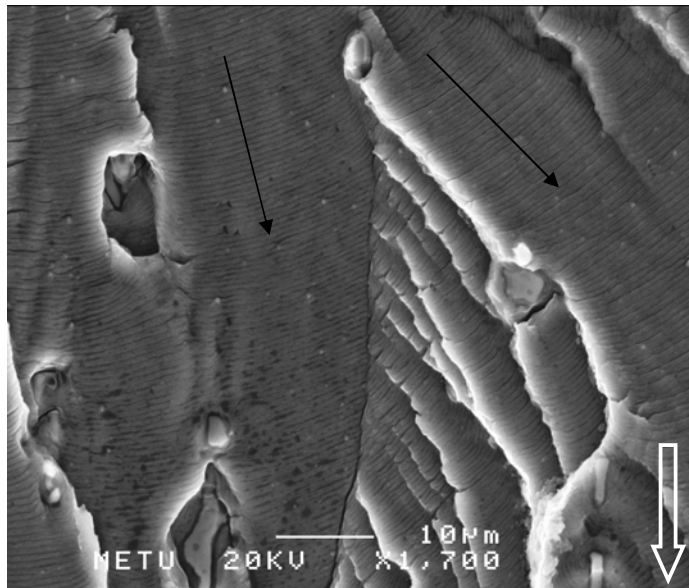
(b)

Figure 4.33. SEM photographs of different specimens.

- a) Intergranular cracking in the high stress intensity zone in TOA T-L specimen. The dimples on the grain boundary facets are the main distinguishing feature of intergranular fracture with microvoid coalescence.
- b) Fatigue striations T651 T-L specimen, black arrows shows local microcracks propagating in different ways.



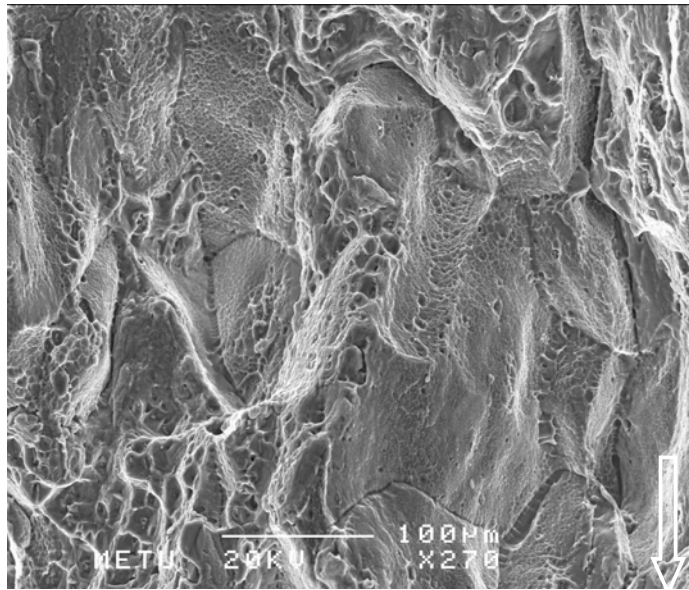
(a)



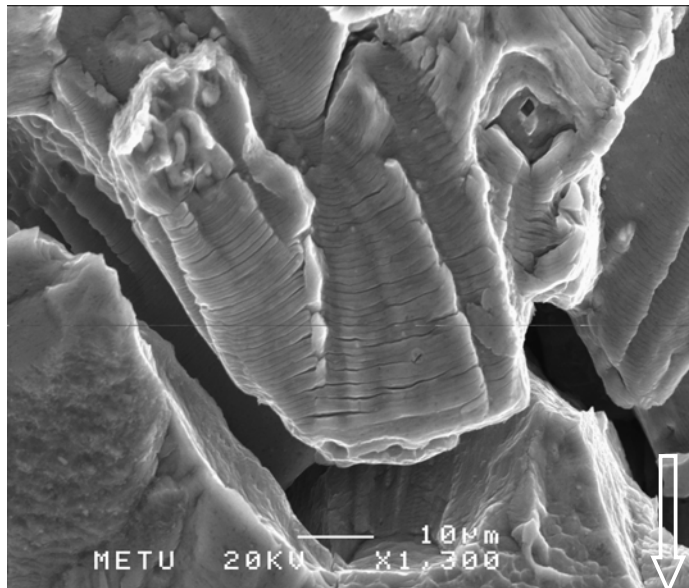
(b)

Figure 4.34. SEM photographs of TOA L-T specimen.

- a) Striations near to the precrack zone.
- b) Coalescence of tear ridges in river pattern, striations indicate two different direction of microcrack growth.



(a)



(b)

Figure 4.35. SEM photographs of TOA L-T specimen.

- a) Dimples on the fracture surface near fast fracture zone.
- b) A large secondary crack.

Examination of the fracture surfaces by SEM shows that transgranular type of crack propagation is dominant through the low and medium fatigue crack growth rate regions, but in the faster zones and in the unstable crack growth zones intergranular fracture in some of the specimens was also observed. Through the fracture surfaces of all specimens, striations, tear ridges, dimples and secondary cracks were observed, which are typical indicators of fatigue. While striations and tear ridges indicate transgranular brittle behavior, as the stress intensity increases dimples were observed which are cluing the ductile fracture.

From the micrographs fatigue crack growth rates were calculated and those in the stage II region are in correlated with the experimental data. The micrographs from fast fracture zone and just before the fast fracture zone give reasonably higher fatigue crack growth rate values.

An intermetallic particle pointed in Figure 4.25(a) and EDS analysis of the particle is shown in Figure 4.36.

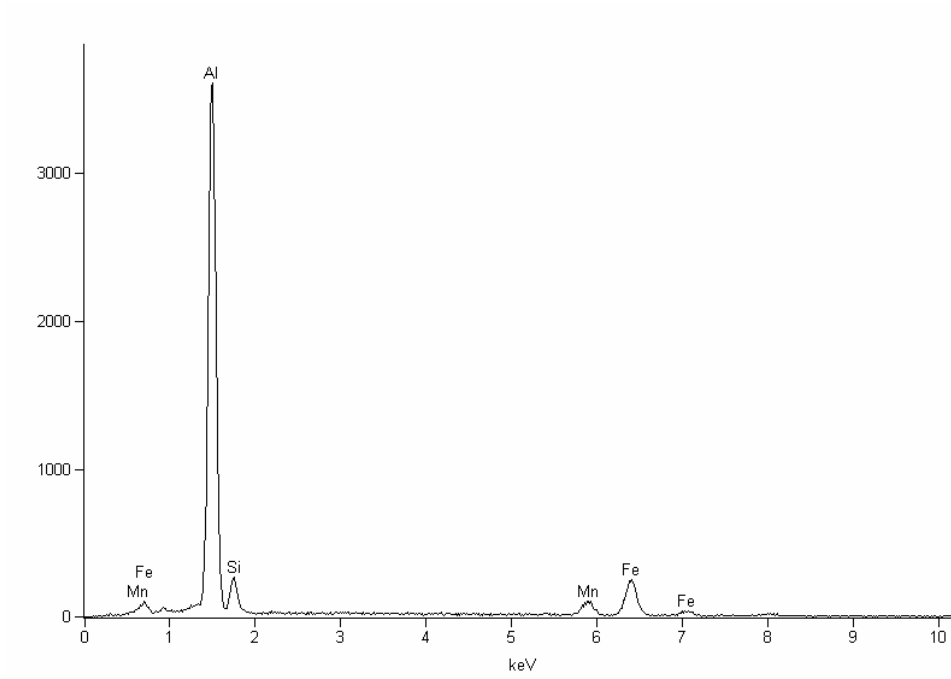


Figure 4.36. EDS analysis of particle in Figure 4.25(a).

Table 4.7. Concentration table of EDS analysis of particle in Figure 4.25(a).

Element	Weight Conc. %	Atom Conc. %	Compound Conc. %	Formula
Al	68.41	78.26	68.41	Al
Si	7.72	8.48	7.72	Si
Mn	6.68	3.75	6.68	Mn
Fe	17.19	9.50	17.19	Fe

EDS analysis is very similar to $\alpha(\text{AlFeMnSi})$ coarse particle with a low Mn/Fe atomic ratio, that Barbosa and his friends also observed and announced before [38].

EDS analysis was made to the particle marked in Figure 4.30(b), it is believed that the particle is the Mg_2Si intermetallic. In Figure 4.37 and Table 4.8, analysis details are shown.

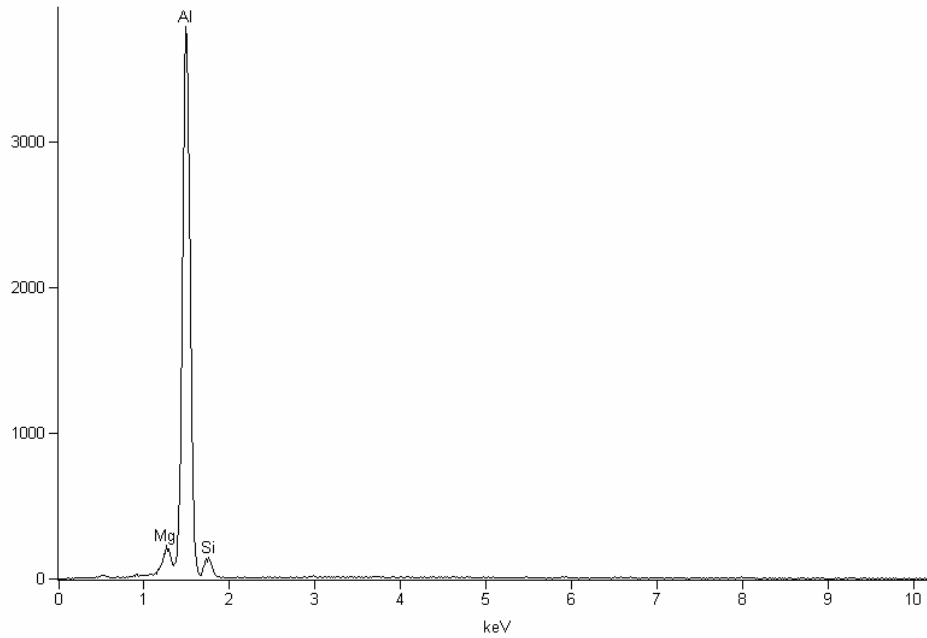


Figure 4.37. EDS analysis of particle in Figure 4.30(b).

Table 4.8. Concentration table of EDS analysis of particle in Figure 4.30(b).

Element	Weight Conc. %	Atom Conc. %	Compound Conc. %	Formula
Mg	2.82	3.13	2.82	Mg
Al	88.94	88.96	88.94	Al
Si	8.24	7.92	8.24	Si

CHAPTER 5

CONCLUSIONS

The aim of this study was to investigate the effect of aging on the fatigue crack growth behavior of a heat treatable, medium strength Al-Mg-Si-Cu aluminum alloy, AA6013.

From the results of aging treatments, fatigue crack growth rate tests and microstructural analysis, following conclusions may be drawn:

1. Orientation of the rolled material affects the fatigue crack growth behavior. It is more resistant to fatigue crack growth in L-T direction for naturally aged and overaged conditions. For the peak aged T651 condition fatigue crack growth resistance is better in T-L direction.
2. The highest fatigue crack growth resistance in T-L direction is obtained in peak aged T651 condition; overaging decreases the resistance of fatigue crack growth in T-L direction.
3. In L-T direction overaging improves fatigue crack growth resistance so that overaged TOA condition is more resistant to fatigue crack growth than naturally aged T42 and peak aged T651 condition.
4. Application of Paris-Erdogan law gives reasonable results at the second stage of fatigue crack growth curves for the all tests of all conditions.

REFERENCES

1. W. Schütz, Engineering Fracture Mechanics, Vol. 54, 1996, pp. 263-300.
2. S. Suresh, "Fatigue of Materials", Cambridge University Press, 1998, pp. 1.
3. R.J. Sanford, "Principles of Fracture Mechanics", Prentice Hall, 2003, pp. 282.
4. www.airdisaster.com/photos/aloha243/7.shtml, 28/07/2006.
5. M. E. Fine, Metall. Trans. A, Vol. 11A, 1980, pp. 368-379.
6. ASM Handbook, Volume 19, "Fatigue and Fracture", pp. 61-210.
7. P. J. E. Forsyth, Proceedings of Cranfield Symposium, 1962, pp.76-94
8. <http://www.key-to-steel.com/Articles/Art162.htm>, 28/07/2006
9. P. Neumann, Acta Metall., Volume 17, 1969, pp. 1219-1225
10. G. Dieter, "Mechanical Metallurgy", McGraw-Hill Book Co., 1988, pp. 396-398
11. J. A. Bannantine, J. J. Comer, J. L. Handrock, "Fundamentals of Metal Fatigue Analysis", Prentice Hall Inc., 1990, pp.100-101
12. P. C. Paris, F. Erdogan, Journal of Basic Engineering, Volume 85, 1961, pp. 528-534
13. S. Suresh, "Fatigue of Materials", Cambridge University Press, 1998, pp. 333
14. A. G. Forman, J. Basic Engineering, Trans. ASME, Series D, Volume 89, 1967, pp. 459-469
15. K. Walker, ASTM STP 462, 1970, pp. 1-14.
16. R. A. Pearson, Engineering Fracture Mechanics., Vol. 7, 1975, pp. 235-247
17. H. L. Ewalds and R. J. H. Wanhill, "Fracture Mechanics", Edward Arnold, 1984, pp. 174.
18. Alcoa, Alloy 6013 Tech Sheet, SPD10-009.
19. Ch. Zamponi, St. Sonneberger, M. Haaks, I. Müller, T. Staab, G. Tempus, K. Maier, Journal Of Materials Science, Vol. 39, 2004, pp. 6951 – 6956.

20. G. Lapasset, Y. Barbaux, Aluminium Alloys for Future Large Aircraft, 1st ONERA-DLR Aerospace Symposium Paris (France), June 21-24, 1999.
21. ASM Handbook, Volume 4, "Heat Treatment", pp. 673-777.
22. E. A. Starke, J.T Staley, Progress in Aerospace Sciences, Vol. 32, 1996, pp. 131-172.
23. ASTM B 209-04, Standard Specification for Aluminum and Aluminum-Alloy Sheet and Plate.
24. SAE AMS 2770G, Heat Treatment of Wrought Aluminum Alloy Parts.
25. SAE AMS 2658B, Hardness and Conductivity Inspection of Wrought Aluminum Alloy Parts.
26. ASTM E 8M-04, Standard Test Methods for Tension Testing of Metallic Materials [Metric].
27. ASTM E 399-90 (Reapproved 1997), Standard Test Method for Plane-Strain Fracture Toughness of Metallic Materials.
28. ASTM E 407-99, Standard Practice for Microetching Metals and Alloys.
29. ASTM E 647-00, Standard Test Method for Measurement of Fatigue Crack Growth Rates.
30. P. C. Paris and B. R. Hayden, A New System for Fatigue Crack Growth Measurement and Control, ASTM Symposium on Fatigue Crack Growth, Pittsburgh, 1979.
31. M. E. Russenberger, Russenberger Prüfmaschinen AG, 7609-16, 1979.
32. P. K. Liaw, H. R. Hartmann and E. J. Helm, Engineering Fracture Mechanics, Vol. 18, No. 1, 1983, pp. 121-131
33. MIL-STD-1537C, Test Method Standard For Electrical Conductivity Test For Verification Of Heat Treatment Of Aluminum Alloys Eddy Current Method, U.S. Department Of Defense, 2002.
34. ASM International Alloy Digest, Alcoa Aluminum Alloy 6013, 1988, A1-282.
35. S. P. Alpay and R. Gürbüz, Script. Metall. Mater., 30, 1994, pp. 423-427.
36. B. E. Amxtutz, M. A. Sutton, D. S. Dawicke and M. L. Boone. ASTM STP 1296, 1997, pp. 105 -125.
37. K. Tanaka, ASTM STP 1020, 1989, pp. 151-183.

- 38.** C. Barbosa, J. M. A. Rebello, O. Acselrad, J. Dille, J. L. Delplancke, Z. Metallkunde, Vol. 93, 2002, pp. 208-211.